Design and Development of Photovoltaic Integrated Grid-tied Active Power Filter With Fuzzy Logic Controllers for Maximum Power Point Tracking and Direct Current Link Voltage Regulation

Arshyn Zhanbolatov, MSc. ECE

Submitted in fulfilment of the requirements for the degree of Master of Science in Electrical and Computer Engineering

School of Engineering and Digital Sciences
Department of Electrical and Computer Engineering Nazarbayev University

53 Kabanbay Batyr Avenue,
Nur-Sultan, Kazakhstan, 010000

Supervisors: Professor Prashant Kumar Jamwal, Professor Muhammad Akhtar

May 2025

DECLARATION

I hereby, declare that this manuscript, entitled "*Design and Development of Photovoltaic Integrated Grid-tied Active Power Filter With Fuzzy Logic Controllers for Maximum Power Point Tracking and Direct Current Link Voltage Regulation*", is the result of my own work except for quotations and citations which have been duly acknowledged.

I also declare that, to the best of my knowledge and belief, it has not been previously or concurrently submitted, in whole or in part, for any other degree or diploma at Nazarbayev University or any other national or international institution.

Name: Arshyn Zhanbolatov
Date: May 2025

Abstract

With growing carbon emissions, energy demand and share of nonlinear loads, photovoltaic (PV) integrated active power filter (APF) systems are being widely adopted in the power sector as they provide dual benefits of supplying PV generation and enhancing the grid power quality (PQ). Maximum power point tracking (MPPT) and direct current (DC) link voltage regulation control techniques are needed in these systems to maintain maximum PV and APF efficiencies under changing environmental and loading conditions. Performances of conventional perturb and observe (P&O) and proportional-integral (PI) techniques degrade significantly in case of large and rapid fluctuations in the operating conditions making them less suitable for highly dynamic systems. In this MSc thesis, PV integrated grid-tied shunt APF with fuzzy logic controllers (FLCs) for MPPT and DC link voltage regulation are designed and developed to improve the efficiency of the PV system and reduce total harmonic distortions (THDs) of the grid currents under large and rapidly varying environmental and loading scenarios. Type-1 Mamdani fuzzy inference systems with simple 5x5 and 7x7 rule bases and set of trapezoidal and triangular membership functions are used for the FLCs' design. Simulation studies and experimental test were conducted in MATLAB/Simulink and laboratory setup to evaluate and validate the performance of the proposed system and compare it against the system with the P&O and PI controllers. The simulation results show that the proposed FLCs provide more accurate and faster responses compared to the conventional controllers under step changes in the solar irradiance and loading resulting in higher PV efficiency and harmonic compensation capability. The experimental test confirmed that the PV integrated APF was able to supply PV active power to the load and achieve grid current THD from 26.99 % to 4.19 % which is within the 5 % limit specified by the Institute of Electrical and Electronics Engineers (IEEE) 519 standard.

Table of Contents

Chapter 1 - Introduction

1.1. Problem Background

The current energy sector is heavily reliant on fossil fuels. Global carbon emissions from coal-fired power plants are continuing to reach new heights raising concerns over their impact on human health and environment [1]. In order to reduce the emissions, there has been a need for new and environmentally friendly power supply systems comprising diverse renewable energy sources. Furthermore, with the global economic and social development, the energy shortage is becoming a driving force for the accelerated exploration and application of the renewable energy systems [1]. The Earth has extensive renewable potential from solar energy. Thus, solar PV systems are an attractive choice in bridging the demand-supply gap. However, output of a PV system is intermittent and influenced by incident irradiance. Ratio of the output power generation to the incident irradiance identifies the PV system efficiency. Different MPPT techniques are adopted in PV systems for finding optimum operation points to achieve maximum efficiency at the given environmental and loading conditions (Fig. 1.1). Tracking accuracy, speed and cost are important metrics in the evaluation of the MPPT techniques. To this regard, implementation of an accurate, fast, and cost-effective MPPT technique has been a research hot-spot for many years and still remains an active research topic [2-6].

The increasing penetration of nonlinear loads has emerged as another challenge for the power sector. Modern devices including computers, smartphones, TVs, LED systems and batteries are designed to operate on DC and thus require prior rectification of the grid's alternating current (AC) supply. This process results in nonlinear relationship between the grid voltages and currents and introduces PQ issues to the grid in the form of harmonic distortions. IEEE 519 standard defines 5 % as an upper limit for the grid current THD [7]. Any further

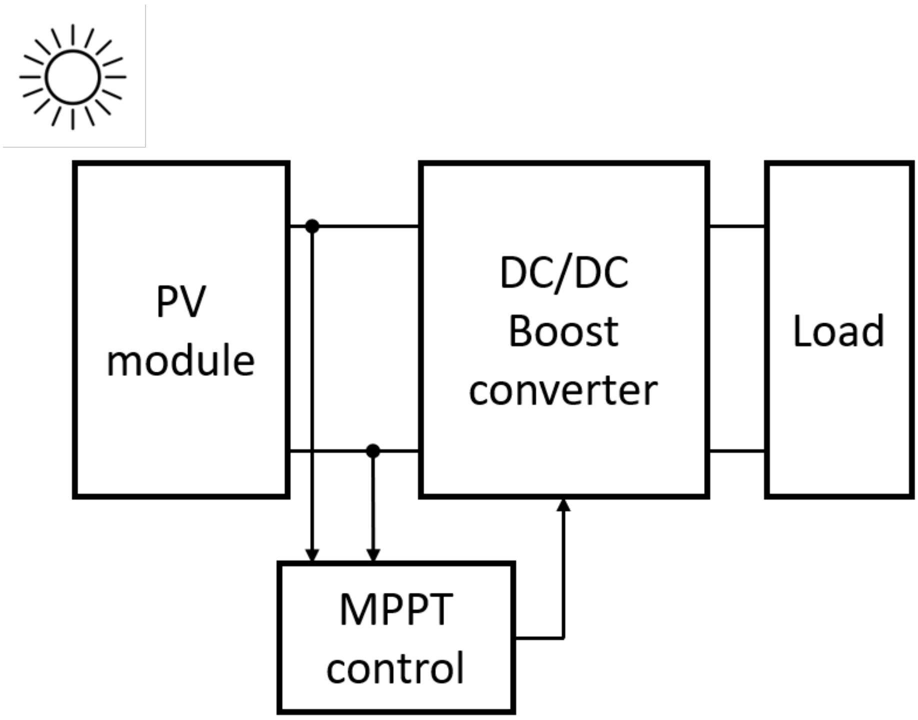

Figure 1.1: PV system with MPPT control.

increase in THD can cause malfunctions in the operation of electrical equipment leading to reduced power efficiency, increased maintenance costs and in severe cases, complete system blackout [8]. Recent advancements in power electronics have stimulated interest in APFs due to their potential to tackle the PQ issues [9]. In a grid-tied scheme, DC output of the PV system can be supplied to AC power grid through inverters (Fig. 1.2). The fundamental idea behind APF is to control the inverters to generate compensation for the undesired grid harmonics. Over the years, different control techniques have been investigated for APFs [10-11]. Among others, control design for DC link voltage regulation has gained wide interest in the research community. Abrupt changes in the power system due to load and PV output variations cause large fluctuations in the DC link that adversely affect the harmonic compensation capability of the APFs and undermine stability of the system. The control technique should be designed with fast and accurate transient response to be able to react to abrupt changes in the operating conditions and recover the voltage level within the specified limits [10].

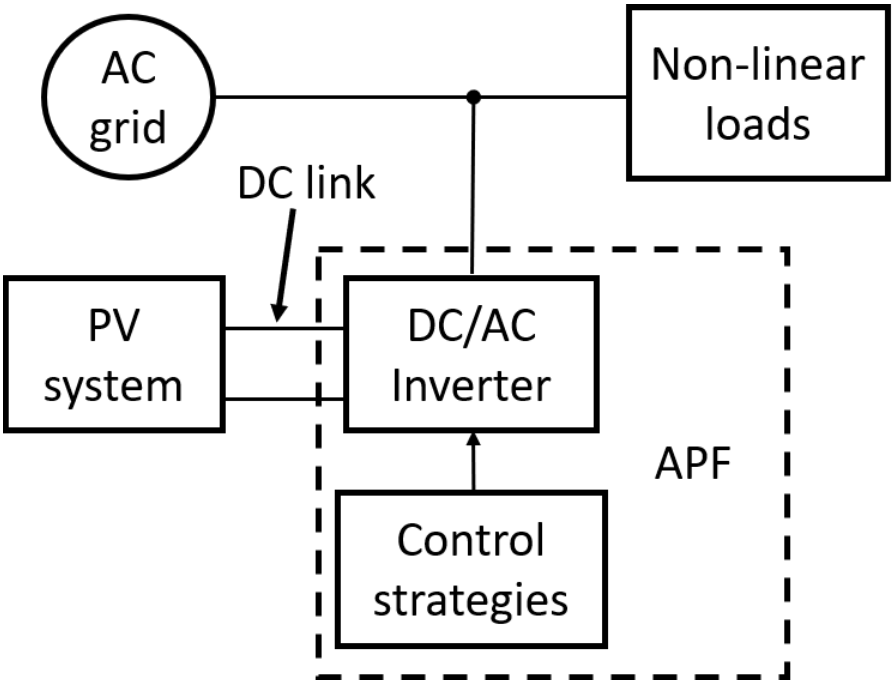

Figure 1.2: PV integrated grid-tied APF system.

1.2. Literature Review

1.2.1. Maximum Power Point Tracking in Photovoltaic Systems

The control techniques based on the P&O algorithm are conventionally adopted for MPPT owing to their simple design and implementation efficiency. As can be seen from Fig. 1.3, its working principle involves iteratively and incrementally adjusting the PV voltage and observing the corresponding variations until the maximum power point (MPP) is reached. However, as pointed out by Bollipo et al. [2], it is prone to oscillations around the MPP, which result in increase in power losses and decrease in accuracy. To tackle the latter, various techniques have been developed that work by adjusting the PV operating point to maintain a constant incremental conductance (INC) [12-14]. The results show their ability to suppress the oscillations at the MPP and improve the tracking efficiency. However, performances of both techniques degrade significantly in case of rapid fluctuations in the operating conditions making them less suitable for highly dynamic environments [4-5].

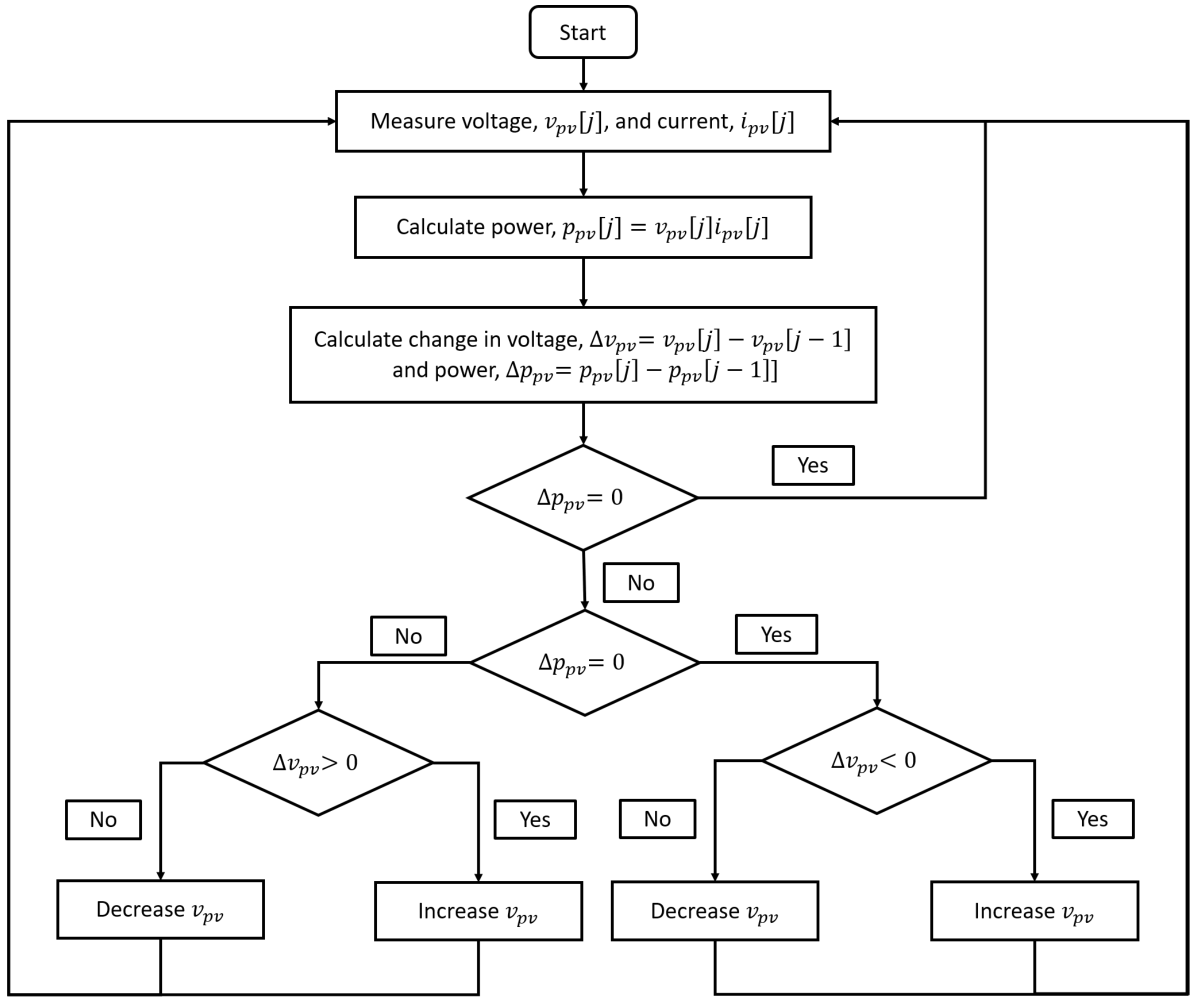

Figure 1.3: Flowchart for the P&O algorithm.

Techniques based on intelligent optimization algorithms such as particle swarm [15], grasshopper [16], and fire fly [17] have demonstrated high performance under dynamic weather and loading conditions. However, they are relatively complex, highly reliant on parameter selection and are subject to convergence issues [6]. Model predictive control (MPC) is a set of sophisticated techniques that can adapt to rapidly changing conditions by predicting future system behavior based on mathematical modeling [18-19]. Study by Ahmed et al. [20] reveals the dependency of their accuracies on the level of details used to describe the system with higher accuracy requiring more detailed models. As a result, MPC requires significantly more intensive computations compared to other techniques for the same level of accuracy.

1.2.2. Direct Current Link Voltage Regulation in Active Power Filters

PI is a traditional control technique that has found wide usage in many applications, including APFs. In the context of DC link regulation, it comprises a feedback loop with proportional and integral blocks that generates a control signal based on the discrepancy between the measured and reference voltages. The control signal is then fed to the APF modulation stage to supply the compensating energy to the DC link. PI-based closed loop voltage control in APF has been studied in [21-27]. However, in all cases the tuning was done off-line according to the pre-defined model of the systems and thus did not consider dynamic changes in the system. References [28-29] applied PSO and GWO algorithms to fine tune the PI parameters to further improve its performance. A study by Bosch et al. [30] incorporated current MPC in order to automatically calibrate the PI parameters in response to the changes in the system dynamics making the voltage control more robust to variations in the system, but at the expense of increased computational burden.

1.2.3. Control Techniques Based on Artificial Intelligence

With recent advancements in artificial intelligence (AI), application of neural networks and fuzzy logics in MPPT and DC link regulation have gained popularity among the research community [31-36]. Table 1.1 provides a summary of the recent works on AI-based MPPT and DC link voltage regulation control for PV integrated APFs. The works based on neural networks show great potential in providing precise dynamic control by learning from historical data. However, the development and integration of neural networks can be challenging due to the need of extensive training data, which is especially important in complex systems with wide range of variability. Due to their ability for intuitive decision-making in uncertain or imprecise environments, FLC-based techniques offer comparable degree of accuracy, speed and adaptability without the need for detailed system model and extensive training data. Although

Table 1.1: Recent works on AI-based MPPT and DC link voltage regulation

Ref.	MPPT control	DC link voltage regulation	Experimental validation
[31]	P&O	Artificial Neural Network	✗
[32]	INC	Delta-Bar-Delta Neural Network	✓
[33]	Hill Climbing Optimization	Neural Network + Normalized Kernel Least Mean Fourth	✓
[34]	FLC	Adaptive Linear Neuron + Unit Vector Template	✗
[35]	FLC	Robust Extended Complex Kalman Filter	✗
[36]	P&O	FLC	✗

FLCs have been independently implemented for MPPT and DC link voltage regulation, to the best of the author's knowledge no previous work is present in the literature that has simultaneously integrated FLCs for both MPPT and DC link voltage regulation in a PV-integrated APF system. Therefore, there is a need for analysis of the performance of such a scheme to fill the research gap. In addition, the claims on the performances of the FLCs in the existing works are often based on simulation results. Thus, further validations in practical experiments are needed to better access their operation.

1.3. Thesis Aims and Objectives

In this MSc thesis, a PV integrated grid-tied APF system is designed and developed to provide dual benefits of supplying PV power to nonlinear loads and generating compensation for the grid current harmonic distortions. Two simple FLCs for MPPT and DC link voltage regulation are proposed to maximize the PV system efficiency and reduce the fluctuations in the DC link under dynamic conditions. The work provides detailed description of the design considerations for the power circuit components and control logics. Simulation studies are done in MATLAB/Simulink for comparative performance analysis of the proposed FLCs against the conventional P&O and PI controllers in terms of response accuracy and speed and the resultant PV and APF efficiencies in the scenarios with step changes in solar irradiance and loading. Experimental tests are carried out in a laboratory setup to validate the operation of the developed PV integrated grid-tied APF system and confirm its compliance with the IEEE 519 standard.

1.4. Thesis Structure

The structure of the MSc thesis is as follows. Chapter 2 gives description of the proposed PV integrated APF system including the design considerations for the power circuit components and control methods. The simulation model and results are presented and discussed in Chapter 3, while experimental setup and validation is included in Chapter 4. Finally, Chapter 5 provides concluding remarks and future directions for research.

Chapter 2 - Methodology

2.1. Overall System

Fig. 2.1. depicts the schematic diagram of the proposed system. It comprises

- an ideal three-phase source representing the grid,
- a three-phase uncontrolled diode bridge rectifier connected to RL load representing the nonlinear loads,
- a PV module with boost converter representing the PV system,
- a three-phase voltage source inverter representing shunt APF
- and the proposed controller block for PV MPPT and APF DC link regulation and source current harmonic mitigation.

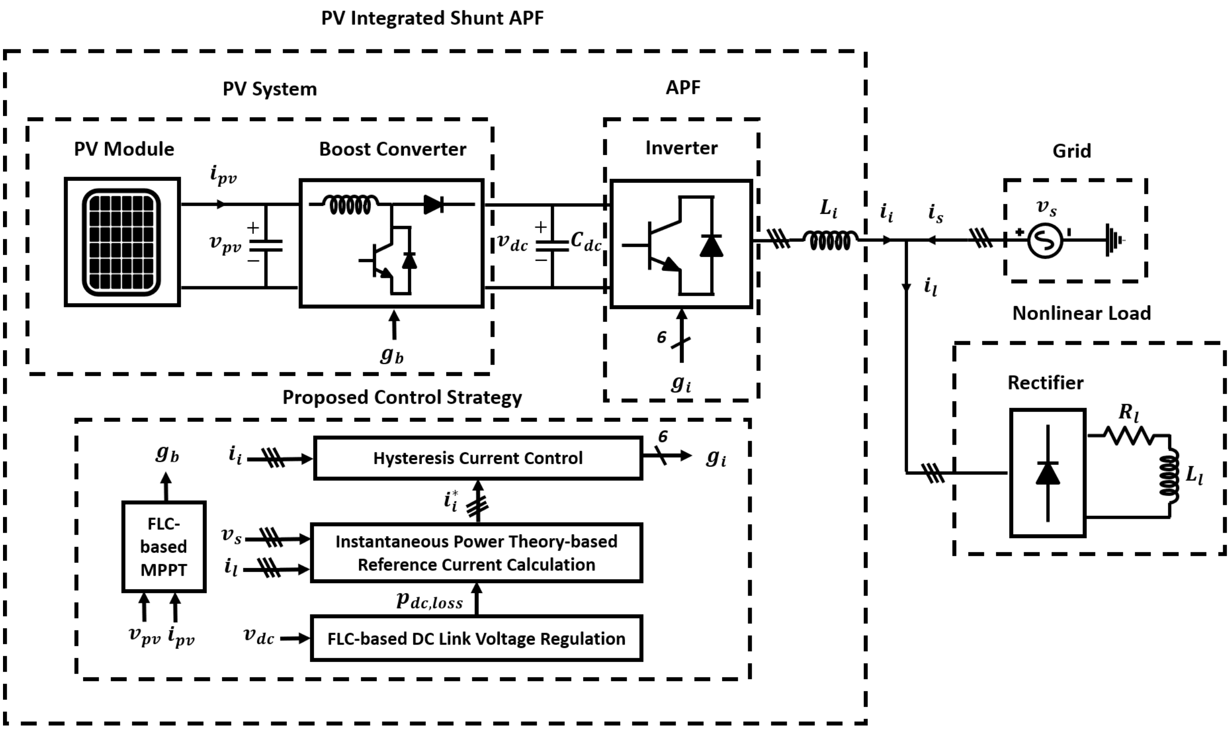

Figure 2.1: Schematic diagram of the proposed system

2.2. Nonlinear Load

The schematic circuit diagram of the three-phase uncontrolled diode bridge rectifier connected to a resistor-inductor (RL) load is illustrated in Fig. 2.2. It consists of six diodes.

The conduction order of the diode pairs are as follows: D1-D6, D6-D3, D3-D2, D2-D5, D5-D4, and D4-D1. Hence, the normalized conduction interval of each diode is $\frac{2\pi}{3}$ radians.

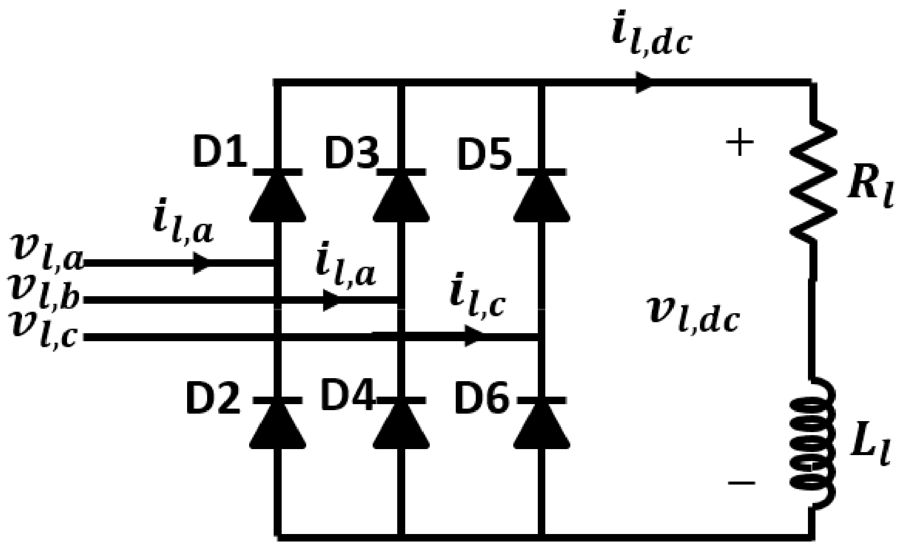

Figure 2.2: Schematic circuit diagram of the three-phase uncontrolled diode bridge rectifier.

Fig. 2.3 shows the operational waveforms of the rectifier under the assumptions of ideal diode characteristics, balanced and undistorted AC voltages, $v_{l,abc}$, and ripple free DC current, $i_{l,dc} = I_{l,dc}$.

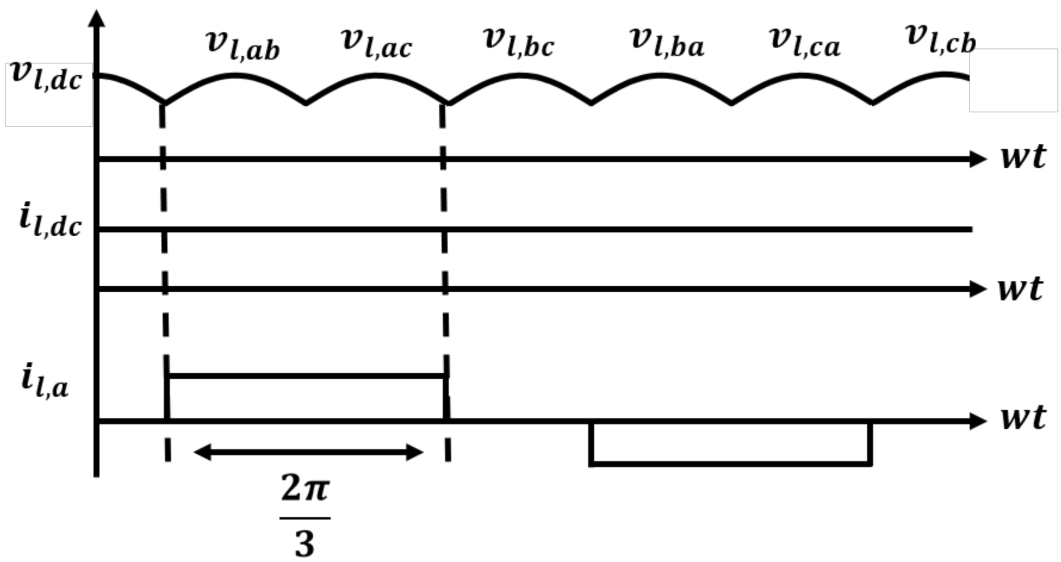

Figure 2.3: Simplified operational waveforms of the three-phase uncontrolled diode bridge rectifier.

Under these assumptions, $I_{l,dc}$ can be expressed by eq. (2.1) where $V_{l,abc}$ is root mean square (RMS) of the $v_{l,abc}$ and R_l is resistance of the load.

$$I_{l,dc} = \frac{3\sqrt{2}V_{l,abc}}{\pi R_l} \tag{2.1}$$

The average active power demand, P_l, is then calculated according to the eq. (2.2).

$$P_l = I_{l,dc}^2 R_l \tag{2.2}$$

Eq. (2.3) and eq. (2.4) give the RMS values of the AC currents, $I_{l,abc}$, and their harmonics, $I_{l,abc,h}$, respectively, where h is the order of the harmonic component.

$$I_{l,abc} = \frac{\sqrt{2}I_{l,dc}}{\sqrt{3}} \tag{2.3}$$

$$I_{l,abc,h} = \frac{2\sqrt{3}I_{l,dc}}{\pi h} \qquad h = 1,5,7,11,13 \ldots \tag{2.4}$$

In this context, the first order harmonic ($h = 1$), referred to as fundamental, corresponds to the desired undistorted sinusoidal current, while the rest ($h > 1$) are the undesired harmonics that need to be compensated. The THD of the AC currents can be computed as the ratio of the RMS values of the undesired harmonics to that of the fundamental one (eq. (2.5)).

$$THD_{i_l} = \frac{\sqrt{I_{l,abc}^2 - I_{l,abc,1}^2}}{I_{l,abc,1}^2} \tag{2.5}$$

2.3. Photovoltaic system

2.3.1. Photovoltaic module

The PV module comprises parallel and series connections of electronic devices, often referred to as PV cells, that convert energy from the light directly into electrical energy by means of the photovoltaic effect. A PV cell can be described using the standard single diode model shown in Fig. 2.4 where i_{ph} is photocurrent that is a function of incident irradiance, G, and effective temperature, T, and R_{sh} and R_s are shunt and series resistances.

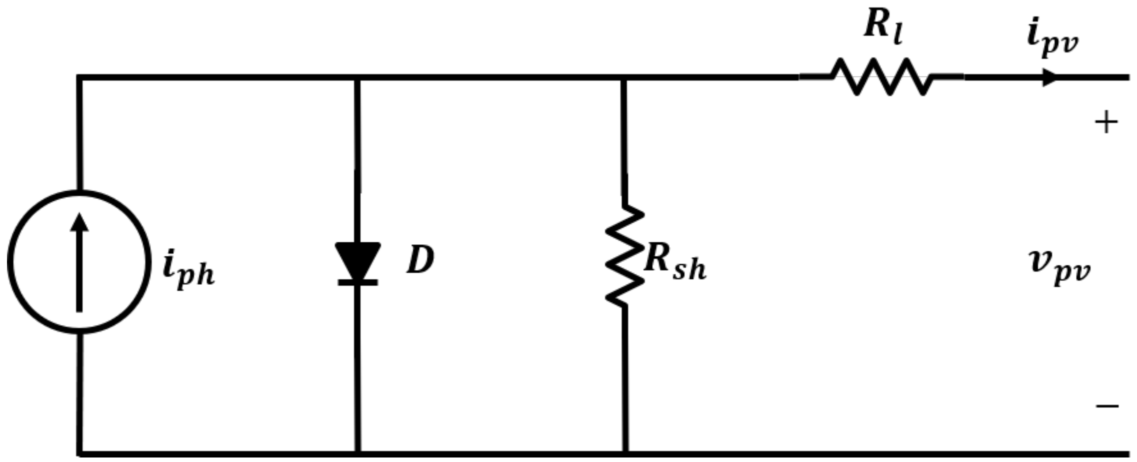

Figure 2.4: Standard single diode model of a PV cell

Using this model and assuming the cells are identical, the I-V equation is expressed mathematically in eq. (2.6) where $i_{d,0}$ and n are the diode reverse saturation current and ideality factor, and q and k are the elementary charge and the Boltzmann's constant, respectively.

$$i_{pv} = i_{ph} - i_{d,0}\left(e^{\frac{q(v_{pv}+R_s i_{pv})}{nkT}} - 1\right) - \frac{v_{pv} + R_s i_{pv}}{R_{sh}} \tag{2.6}$$

The Fig. 2.5 illustrates typical PV I-V and P-V curves where $I_{pv,sc}$ is short-circuit value of i_{pv}, $I_{pv,mpp}$ is value of i_{pv} at MPP, $V_{pv,oc}$ is open-circuit value of v_{pv}, $V_{pv,mpp}$ is value of v_{pv} at MPP, $p_{pv} = i_{pv}v_{pv}$ and $P_{pv,mpp}$ is the value of p_{pv} at MPP. It can be inferred from eq. (2.6) that the PV I-V and P-V characteristics are influenced by i_{ph} which in turn is a function of G. Thus, MPP does stay fixed in position and shifts with the changes in the G. For designing the components of the PV system, typically rated values of $I_{pv,mpp}$ and $V_{pv,mpp}$ are used that are obtained at standard test conditions (STC) i.e., $T_{stc} = 25^{\circ}C$, $G_{stc} = 1\ kW/m^2$ and 1.5 air mass.

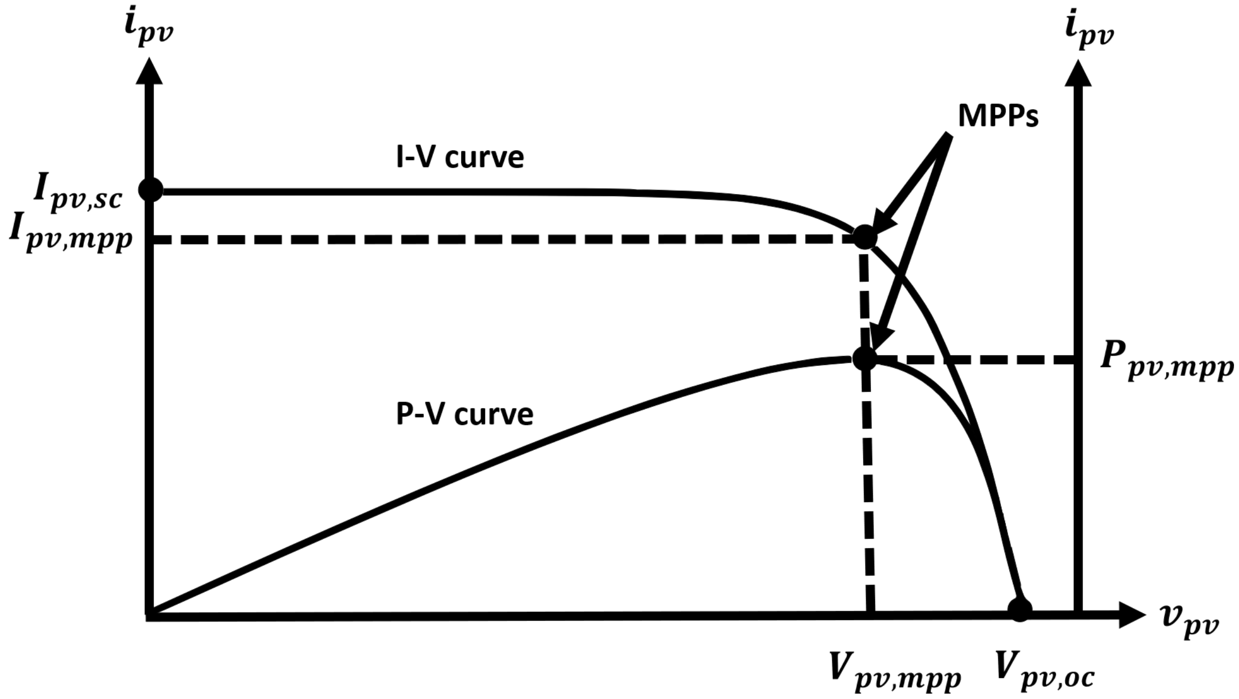

Figure 2.5: PV I-V and P-V curves

2.3.2 Boost Converter

The electrical energy from the PV module is injected to the inverter by a DC-DC boost converter. It comprises an inductor, a switch and a diode which are connected to the DC-link capacitor. The schematic diagram of the converter is illustrated in Fig. 2.6 where i_L is current through the inductor, L_b is inductance value of the inductor, g_b is gate signal to the switch, C_{dc} is output DC-link capacitance, and i_{dc} is output DC link current.

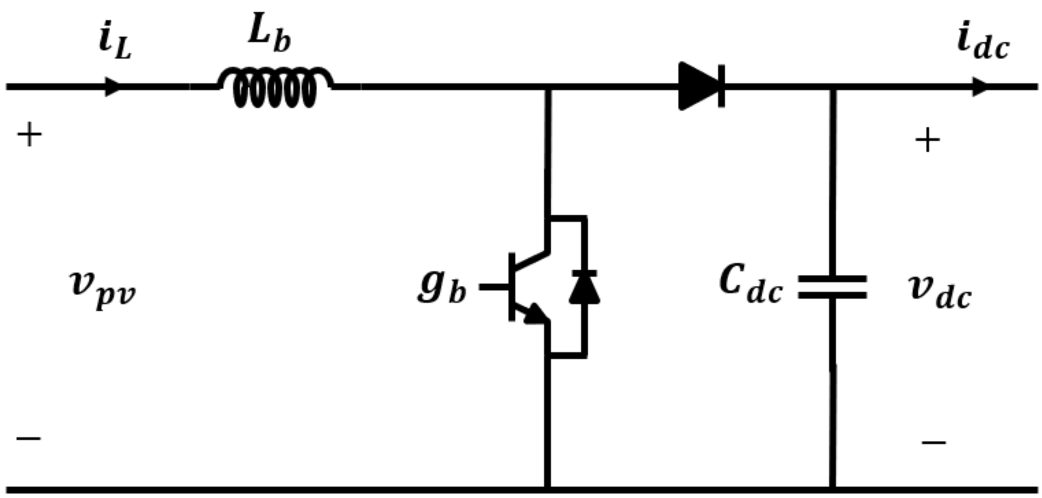

Figure 2.6: Schematic circuit diagram of the DC-DC boost converter.

The DC-DC boost converter can be set to function in either continuous conduction mode (CCM) or discontinuous conduction mode (DCM). In the former, the operation in each switching period can be separated into two intervals: when the switch is closed i.e., $g_b = 1$, and when the switch is open i.e., $g_b = 1$. Fig. 2.7 shows equivalent schematic circuit diagram of the converter during the time that the switch is closed assuming ideal circuit elements. In this case, the input energy is accumulated in the inductor whereas the i_{dc} is provided by the capacitor.

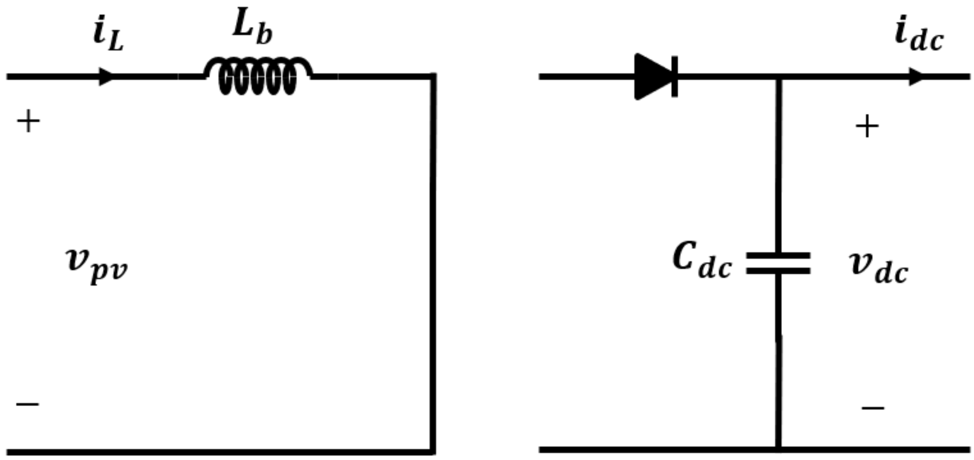

Figure 2.7: Equivalent schematic circuit diagram of the converter during the time that the switch is closed.

Fig. 2.8 shows equivalent schematic circuit diagram of the converter during the time that the switch is open. In this case, the inductor supplies the accumulated energy to the output capacitor and inverter. Fig. 2.9 depicts the operational waveforms of the converter during complete switching cycle where f_b is the switching frequency and D is the proportion of the switching period when it is closed, also referred to as duty cycle. The average relation of the input and output voltages is expressed in terms of the D (eq. (2.7)).

$$v_{pv} = (1 - D)v_{dc} \tag{2.7}$$

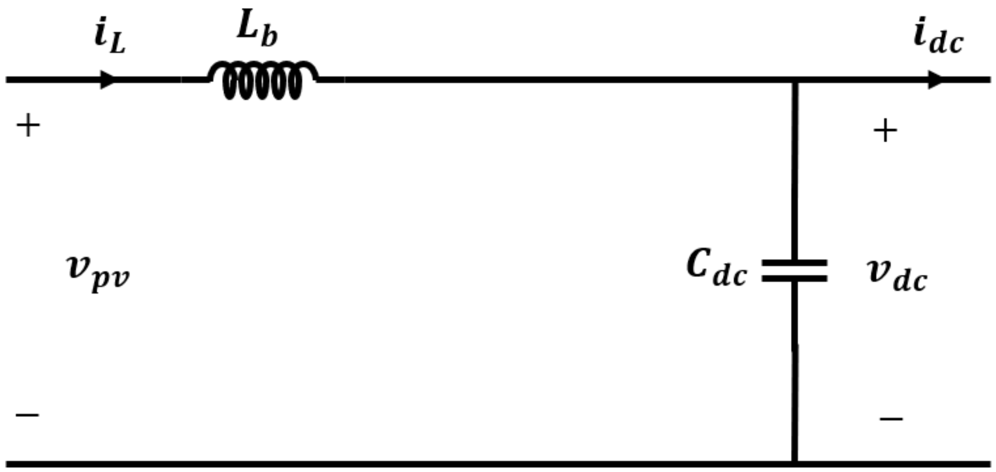

Figure 2.8: Equivalent schematic circuit diagram of the converter during the time that the switch is open.

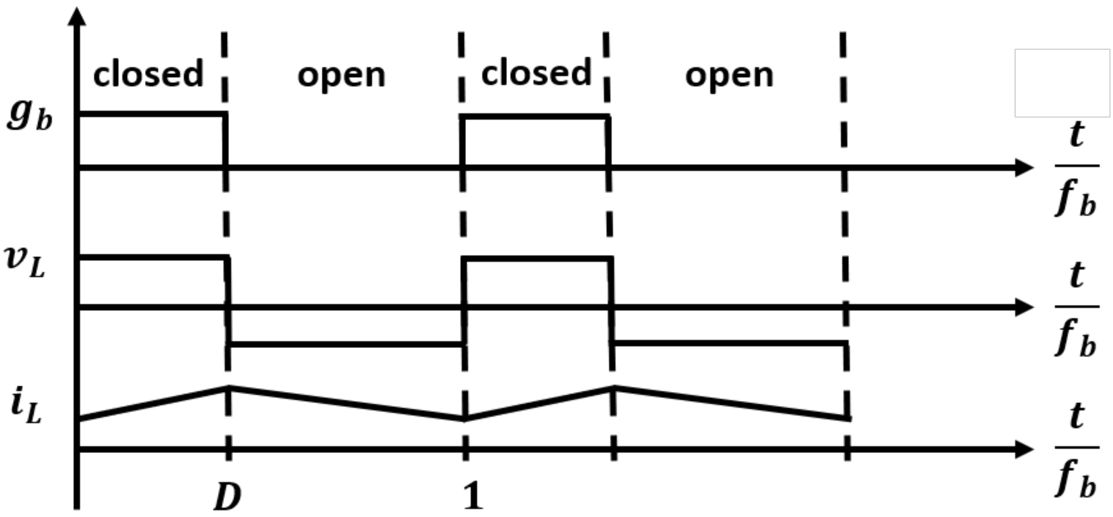

Figure 2.9: Operational waveforms of the converter in CCM.

Fig. 2.10 depicts the operational waveforms of the converter in DCM. In this mode, the flow of current across the inductor is discontinuous since i_L drops to zero before the start of the subsequent switching period. It is desirable to operate the boost converter in CCM since it gives smoother and more predictable current and voltage waveforms and thus enables more efficient MPPT. The minimum inductance to ensure CCM operation is given by eq. (2.8)

$$L_{b,min} = \frac{D(1-D)^2 v_{dc}}{2 f_b i_{dc}} \tag{2.8}$$

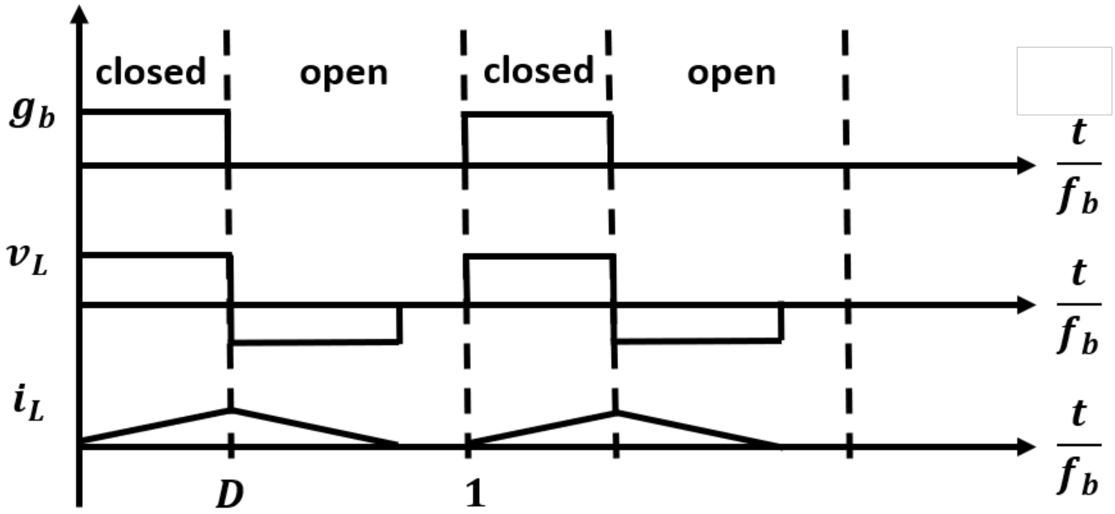

Figure 2.10: Operational waveforms of the converter in DCM.

In practice, inductance much higher than $L_{b,min}$ is required due to input current ripple and maximum output current specifications. A good estimation for the L_b can be obtained using eq. (2.9) where $V_{pv,mpp,stc}$ is the rated PV module voltage, V_{dc}^* is the reference DC link voltage, and Δi_L is the desired inductor current ripple [37].

$$L_b = \frac{V_{pv,mpp,stc}(V_{dc}^* - V_{pv,mpp,stc})}{\Delta i_L f_b V_{dc}^*} \tag{2.9}$$

In order to obtain maximum efficiency at different irradiance levels, the v_{pv} is maintained at $v_{pv.mpp}$ by controlling D through g_b. In this MSc thesis, FLC is used to track the MPP and generate the corresponding g_b.

2.3.3. Fuzzy Logic Controller-Based Maximum Power Point Tracking

Fig. 2.11 shows the proposed controller block diagram for the FLC-based MPPT. The inputs to the FLC are the rate of change of p_{pv} with respect to v_{pv} (eq. 2.10) and the change in the rate of change (eq. 2.11).

$$O_{pv}[j] = \frac{p_{pv}[j] - p_{pv}[j-1]}{v_{pv}[j] - v_{pv}[j-1]} \tag{2.10}$$

$$\Delta O_{pv}[j] = O_{pv}[j] - O_{pv}[j-1] \tag{2.11}$$

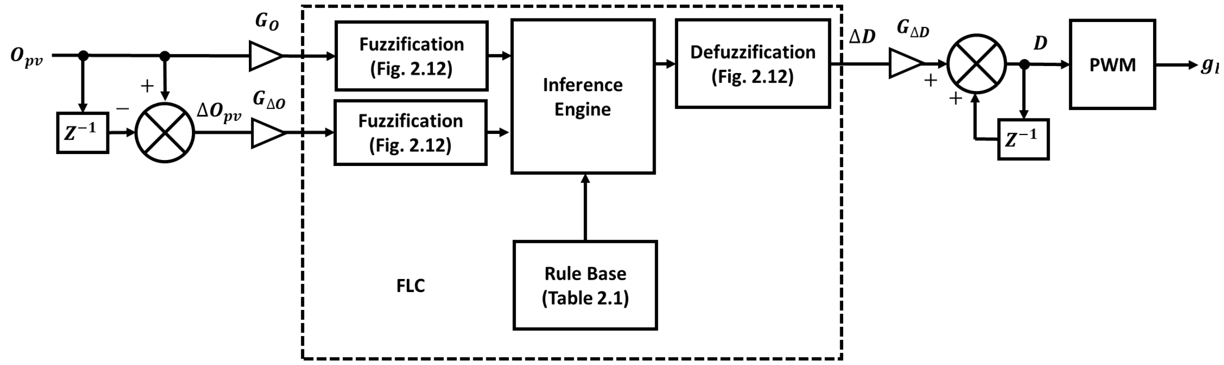

Figure 2.11: Controller block diagram for MPPT

The output of the FLC is the increase in the boost converter duty cycle (eq. (2.12)).

$$\Delta D[j] = D[j] - D[j-1] \tag{2.12}$$

Type-1 Mamdani fuzzy inference system is adopted in this MSc thesis since it offers high degree of flexibility in representing relationships between inputs and outputs under complex system dynamics and is most commonly used in the literature [38]. Fuzzification and defuzzification are done by using combination of triangular and trapezoidal membership functions due to computational efficiency and ease of implementation. “Min” and “max” methods are used for “AND” and “OR” operations during fuzzification, and centroid of area method is used during defuzzification. A 5x5 rule base with 5 membership functions for each input is adopted since it is found to be sufficient to characterize the mapping between the input and output variables and increasing the number of membership functions beyond that will increase the computational complexity of the FLC. Generally, designing Mamdani fuzzy inference system require intuitive knowledge of the system behavior. In this MSc thesis, rule-base and membership function ranges are first formulated from the systematic design steps recommended in [39]. Then, further fine tuning of the input and output gains, G_O, $G_{\Delta O}$ and $G_{\Delta D}$, is done based on the analysis of the results from the P&O algorithm and through trial and error to reach desired performance targets. Fig. 2.12 and Table 2.1 show the obtained membership functions and rule base where “+”, “-”, “N”, “L” and “H” stand for positive, negative, no, low and high changes in the variables, respectively.

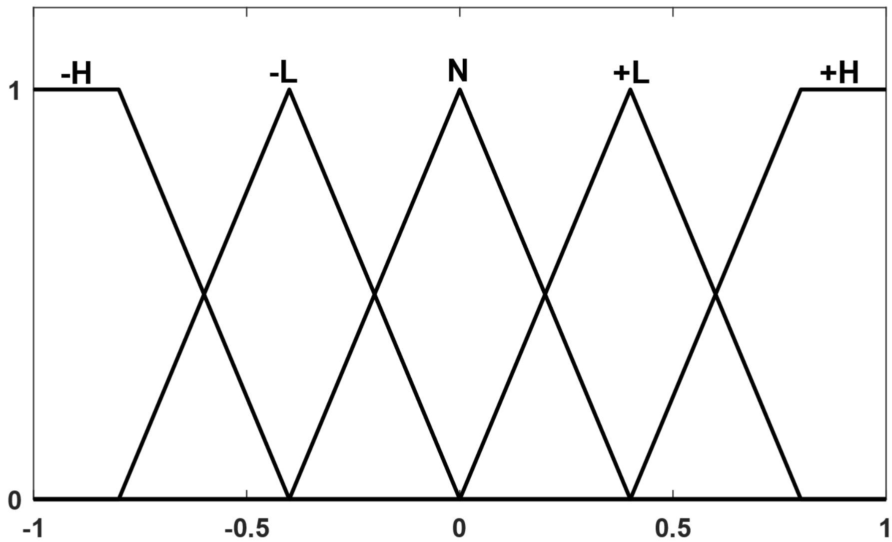

Figure 2.12: FLC membership functions of input and output variables for MPPT

Table 2.1: FLC rule base for MPPT

O_{pv} \ ΔO_{pv}	**-H**	**-L**	**N**	**+L**	**+H**
-H	N	+H	+H	+H	+H
-L	+H	+L	+L	N	N
N	+L	N	N	N	-L
+L	N	N	-L	-L	-H
+H	+H	N	-L	-H	N

2.4. Active Power Filter

2.4.1. Inverter

Fig. 2.13 depicts the schematic circuit diagram of the three-phase voltage source inverter with the input DC-link capacitor and output AC line interfacing inductors.

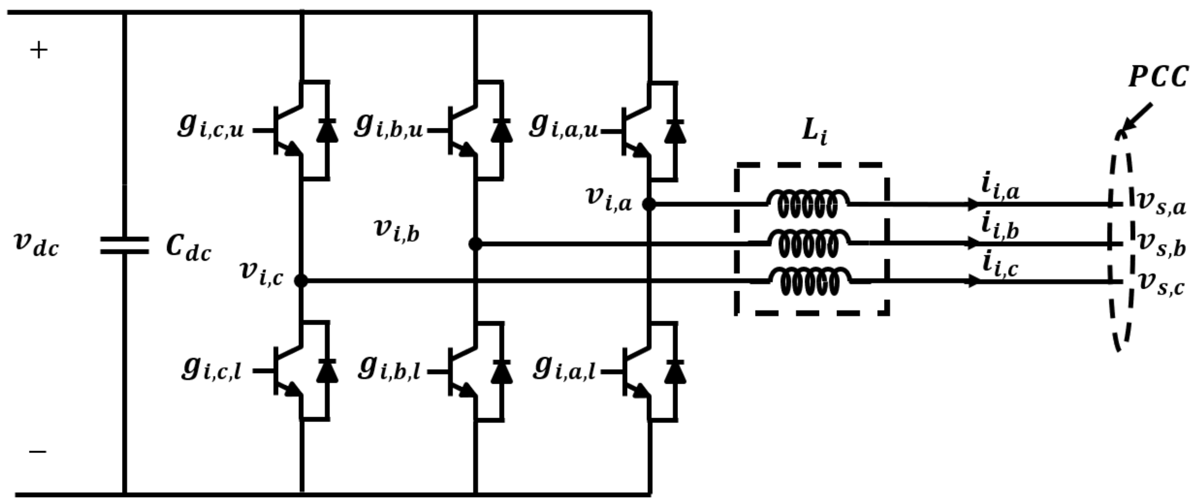

Figure 2.13: Schematic circuit diagram of the three-phase voltage source inverter

A half-bridge inverter topology with three-legs and six switches is adopted. The upper and lower switches in each leg are complementary as shown in eq. (2.13-15) where $g_{i,a,u}$, $g_{i,a,l}$, $g_{i,b,u}$, $g_{i,b,l}$, $g_{i,c,u}$, and $g_{i,c,l}$ are the gate signals to the switches.

$$g_{i,a,u} + g_{i,a,l} = 1 \tag{2.13}$$

$$g_{i,b,u} + g_{i,b,l} = 1 \tag{2.14}$$

$$g_{i,c,u} + g_{i,c,l} = 1 \tag{2.15}$$

In general, the inverter has eight switching states that are tabulated in Table 2.2 where $v_{i,ab}$, $v_{i,bc}$, and $v_{i,ca}$ are the phase to phase voltages at the inverter output terminals.

Table 2.2: Switching states of the three-phase voltage source inverter

$g_{i,a,u}$	$g_{i,b,u}$	$g_{i,c,u}$	$v_{i,ab}$	$v_{i,bc}$	$v_{i,ca}$
0	0	0	0	0	0
0	0	1	0	$-v_{dc}$	v_{dc}
0	1	0	$-v_{dc}$	v_{dc}	0
0	1	1	$-v_{dc}$	0	$-v_{dc}$
1	0	0	v_{dc}	0	$-v_{dc}$
1	0	1	v_{dc}	$-v_{dc}$	0
1	1	0	0	v_{dc}	$-v_{dc}$
1	1	1	0	0	0

It can be seen that the resulting phase to phase voltages have three discrete levels: $-v_{dc}$, 0 and v_{dc}. Due to the voltage drop at the coupling inductors, L_i, the inverter needs to maintain $v_{i,ab}$, $v_{i,bc}$, and $v_{i,ca}$, higher than the corresponding source voltages at the point of common coupling, $v_{s,ab}$, $v_{s,bc}$, and $v_{s,ca}$, in order to generate the compensating currents, $i_{i,a}$, $i_{i,b}$, and $i_{i,c}$. For this purpose, the minimum allowable DC link voltage level can be calculated using eq. (2.16) where V_s is the phase to phase RMS source voltage [40].

$$v_{dc,min} = \frac{2\sqrt{2}V_s}{\sqrt{3}} \tag{2.16}$$

Thus, V_{dc}^* should be chosen larger than $v_{dc,min}$. During steady-state operation, the v_{dc} is maintained at V_{dc}^* with some ripples. The voltage ripples in DC-link will, in turn, add ripples to the inverter output currents, i_i. Thus, the capacitor should be properly sized in order to maintain the ripple within the required specifications. In this MSc thesis, the DC-link capacitance value is selected according to eq. (2.17) where $P_{l,max}$ is the maximum active power demand of the load and ΔV_{dc} is the allowable DC link voltage ripple [41].

$$C_{dc} = \frac{P_l/V_{dc}^*}{4\pi f_s \Delta V_{dc}} \tag{2.17}$$

2.4.2. Hysteresis Current Control

In order to generate the compensating currents, i_i, the inverter is set to operate in current controlled mode. The hysteresis current controller is used in this MSc thesis. Hysteresis current controller operates by generating gate signals, g_i, to the inverter switches based on the difference between i_i and i_i^*. The control logics for the upper switches are expressed in eq. (2.18-2.20) where HB is a constant hysteresis band.

$$g_{i,a,u} = \begin{cases} 0, & i_{i,a} - i_{i,a}^* < HB \\ 1, & i_{i,a} - i_{i,a}^* \geq HB \end{cases} \tag{2.18}$$

$$g_{i,b,u} = \begin{cases} 0, & i_{i,b} - i^*_{i,b} < HB \\ 1, & i_{i,b} - i^*_{i,b} \geq HB \end{cases} \tag{2.19}$$

$$g_{i,c,u} = \begin{cases} 0, & i_{i,c} - i^*_{i,c} < HB \\ 1, & i_{i,c} - i^*_{i,c} \geq HB \end{cases} \tag{2.20}$$

The Fig. 2.14 shows the hysteresis current control voltage and current waveforms for phase a.

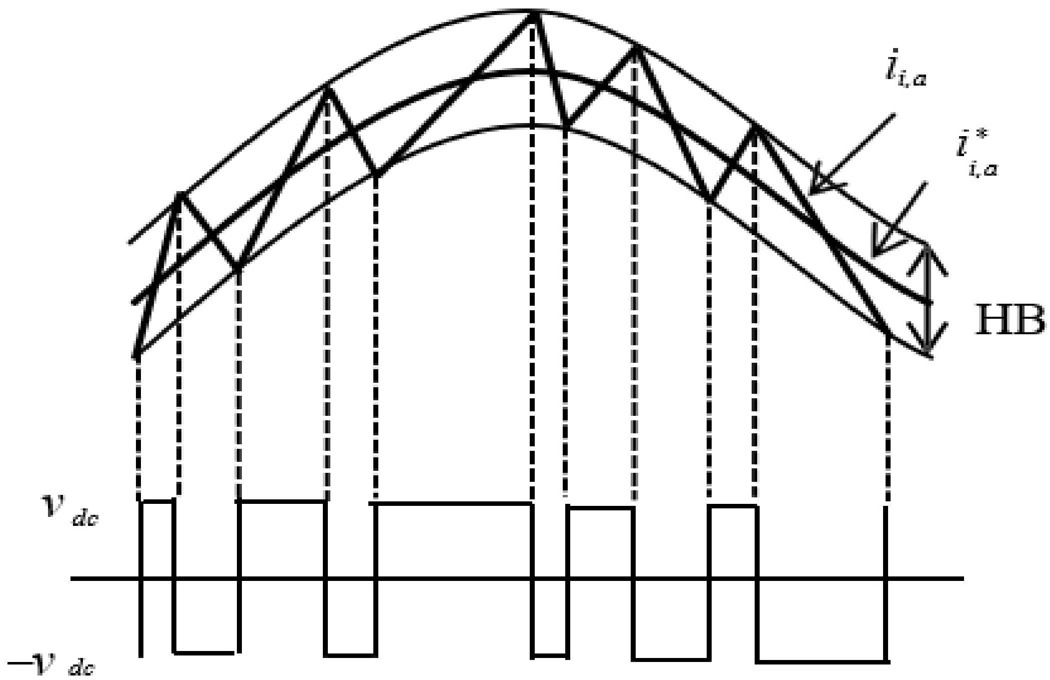

Figure 2.14: Hysteresis current control waveforms for phase a.

In hysteresis current control, the inverter switching frequency, f_i, is determined by the time it takes for $i_{i,a}$ to go from the lower to the upper limit of the HB and vice versa. It can be seen from the Fig. 2.14 that f_i does not remain constant and changes according to the band limits and rate of change of $i_{i,a}$. The latter, in its turn, depends on the DC link voltage and coupling inductors. Generally, small HB and high f_i are desired to decrease the current ripples and increase the transient response of the controller. Given the desired specifications for the inverter switching frequency, hysteresis band and DC link voltage, an estimation for the required sizing of the coupling inductors can be obtained by using eq. (2.21) [42].

$$L_i = \frac{\sqrt{3}V_{dc}^*}{12 f_i HB} \tag{2.21}$$

2.4.3. Reference Current Calculation

Reference current calculation is based on the instantaneous power theory also referred to as p-q theory. First, the source voltages, v_s, and load currents, i_l, in the a-b-c frame are converted to the α-β frame using well-known Clarke transformation (eq. (2.22-2.23)).

$$\begin{bmatrix} v_{s,\alpha} \\ v_{s,\beta} \end{bmatrix} = \sqrt{\frac{2}{3}} \begin{bmatrix} \frac{1}{\sqrt{2}} & \frac{1}{\sqrt{2}} & \frac{1}{\sqrt{2}} \\ 1 & -\frac{1}{2} & -\frac{1}{2} \end{bmatrix} \begin{bmatrix} v_{s,a} \\ v_{s,b} \\ v_{s,c} \end{bmatrix} \tag{2.22}$$

$$\begin{bmatrix} i_{l,\alpha} \\ i_{l,\beta} \end{bmatrix} = \sqrt{\frac{2}{3}} \begin{bmatrix} \frac{1}{\sqrt{2}} & \frac{1}{\sqrt{2}} & \frac{1}{\sqrt{2}} \\ 1 & -\frac{1}{2} & -\frac{1}{2} \end{bmatrix} \begin{bmatrix} i_{l,a} \\ i_{l,b} \\ i_{l,c} \end{bmatrix} \tag{2.23}$$

From these, the instantaneous real and imaginary load powers, p_l and q_l, are computed according to eq. (2.24).

$$\begin{bmatrix} p_l \\ q_l \end{bmatrix} = \begin{bmatrix} v_{s,\alpha} & v_{s,\beta} \\ v_{s,\beta} & -v_{s,\alpha} \end{bmatrix} \begin{bmatrix} i_{l,\alpha} \\ i_{l,\beta} \end{bmatrix} \tag{2.24}$$

The p_l can be separated into its mean, $\overline{p_l}$. and alternating, $\widetilde{p_l}$, parts such that $p_l = \overline{p_l} + \widetilde{p_l}$. Here, the $\widetilde{p_l}$ corresponds to the harmonic component of the $\widetilde{p_l}$. In order to supply the PV power and generate compensation for the undesired harmonics and DC link loss, $p_{dc,loss}$, the reference inverter currents, i_i^*, in α-β frame and subsequently in a-b-c frame are calculated using eq. (2.25) and eq. (2.26), respectively.

$$\begin{bmatrix} i_{i,\alpha}^* \\ i_{i,\beta}^* \end{bmatrix} = \frac{1}{{v_{s,\alpha}}^2 + {v_{s,\beta}}^2} \begin{bmatrix} v_{s,\alpha} & -v_{s,\beta} \\ v_{s,\beta} & v_{s,\alpha} \end{bmatrix} \begin{bmatrix} \widetilde{p_l} + p_{pv} - p_{dc,loss} \\ q_l \end{bmatrix} \tag{2.25}$$

$$\begin{bmatrix} i_{i,a}^* \\ i_{i,b}^* \\ i_{i,c}^* \end{bmatrix} = \sqrt{\frac{2}{3}} \begin{bmatrix} 1 & 0 \\ -\frac{1}{2} & \frac{\sqrt{3}}{2} \\ -\frac{1}{2} & -\frac{\sqrt{3}}{2} \end{bmatrix} \begin{bmatrix} i_{i,\alpha}^* \\ i_{i,\beta}^* \end{bmatrix} \quad (2.26)$$

The controller block diagram for the above steps is shown in Fig. 2.15.

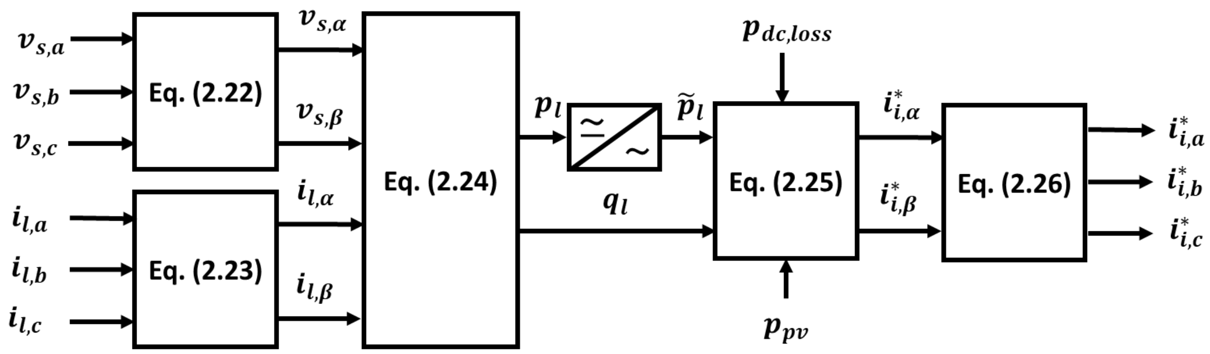

Figure 2.15: Controller block diagram for reference current calculation

2.4.4. Fuzzy Logic Controller-Based Direct Current Link Voltage Regulation

As mentioned earlier, for adequate APF operation, the DC link voltage, v_{dc}, needs to be regulated to remain at the constant reference value, V_{dc}^*. During transient conditions e.g., abrupt changes in the load and PV generation, the differences in the active power supply and demand is supplied by the DC link capacitor. As a result, sudden and large increases (overshoots) or decreases (undershoots) in the v_{dc} levels are introduced. As shown earlier, p-q theory provides means for v_{dc} regulation based on the $p_{dc,loss}$ which corresponds to the power loss at the DC link capacitor C_{dc}. Fig. 2.16 illustrates the block diagram of FLC-based $p_{dc,loss}$ estimation for v_{dc} regulation. As in the case for MPPT, fuzzification and defuzzification are done by using combination of triangular and trapezoidal membership functions due to computational efficiency and ease of implementation. “Min” and “max” methods are used for “AND” and “OR” operations during fuzzification, and centroid of area method is used during defuzzification. For DC link voltage regulation, a 7x7 rule base with 7

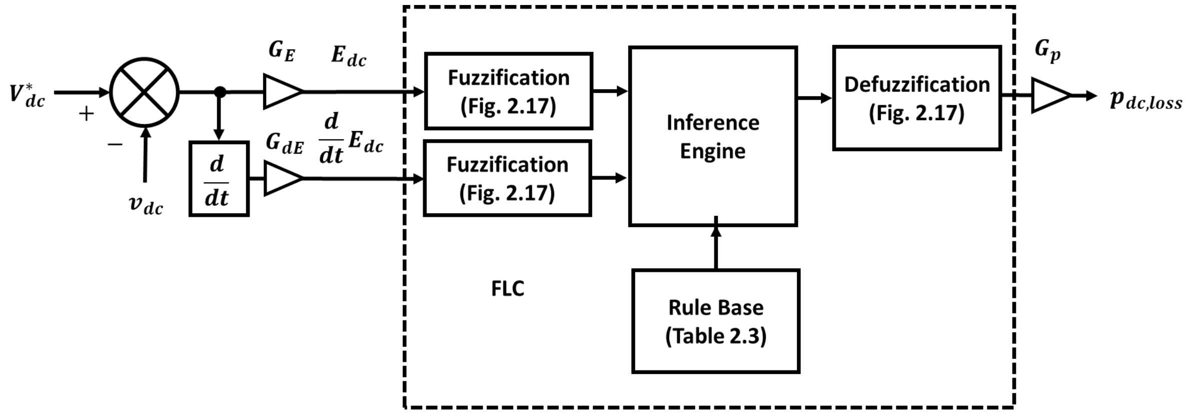

Figure 2.16: Controller block diagram for DC link voltage regulation

membership functions for each input are needed to efficiently capture the highly nonlinear relationships between the input and output variables. Rule-base and membership function ranges are first formulated according to the systematic design steps recommended in [39]. Then, further fine tuning of the input and output gains, G_E, G_{dE} and G_p, is done from the analysis of the results from the conventional PI control and through trial and error to reach desired performance targets. Fig. 2.17 shows the FLC membership functions for input and output variables and Table 2.3 shows the FLC rule base. In this case, “M” stands for moderate changes in the variables.

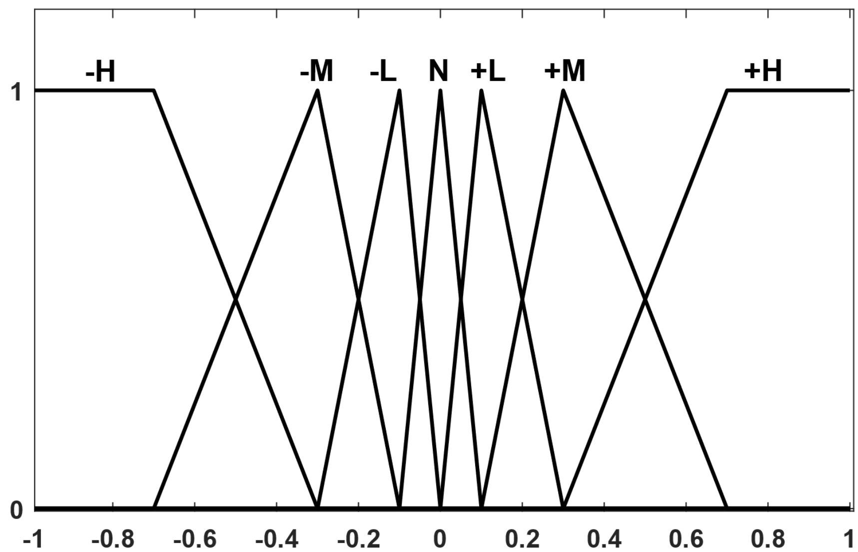

Figure 2.17: FLC membership functions of input and output variables for DC link voltage regulation

Table 2.3: FLC rule base for DC link voltage regulation

E_{dc} \ $\frac{d}{dt}E_{dc}$	**-H**	**-M**	**-L**	**N**	**+L**	**+M**	**+H**
-H	-H	-H	-H	-H	-M	-L	N
-M	-H	-H	-H	-M	-L	N	+L
-L	-H	-H	-M	-L	N	+L	+M
N	-H	-M	-L	N	+L	+M	+H
+L	-M	-L	N	+L	+M	+H	+H
+M	-L	N	+L	+M	+H	+H	+H
+H	N	+L	+M	+H	+H	+H	+H

Chapter 3 – Simulation Study

3.1. System Model Parameters

The simulation studies are carried out in MATLAB/Simulink to analyze and verify the effectiveness of the proposed PV integrated grid-tied APF with FLCs for MPPT and DC link voltage regulation. The implemented Simulink model of the proposed system is depicted in Fig. 3.1. The parameters of the system adopted in the simulation are tabulated in Table 3.1. The power system includes a three-phase grid with $V_s = 400\ V$ phase to phase RMS voltage and $f_s = 50\ Hz$ operating frequency and two nonlinear loads with a combined $P_l = 8.967\ kW$ of active power demand. For the PV system, 2 parallel strings of 6 series SunPower SPR-300E-WHT-D modules are used with resultant rating of $P_{pv,mpp,stc} = 3.603\ kW$. The circuit elements are assumed to be ideal. The parameters and sizes of the components for the DC link, inverter and DC-DC boost converter are calculated according to the design considerations discussed in Chapter 2. Eq. (3.1) shows the calculation of the minimum allowable DC link voltage based on eq. (2.16).

$$v_{dc,min} = \frac{2 \times \sqrt{2} \times V_s}{\sqrt{3}} = \frac{2 \times \sqrt{2} \times 400}{\sqrt{3}} = 653.20\ V \tag{3.1}$$

Thus, the reference DC link voltage is set larger than the $v_{dc,min}$ as $V_{dc}^* = 700\ V$. The DC link capacitance is first calculated in eq. (3.2) according to the energy balance formula in eq. (2.17) to limit the DC link voltage ripples to $1.4\ V$ i.e., $0.2\ \%$ of the V_{dc}^*. However, for practical considerations, it is rounded to the closest accessible capacitator value.

$$C_{dc} = \frac{P_l/V_{dc}}{4\pi f_s \Delta V_{dc}} = \frac{8968/700}{4\pi \times 50 \times 1.4} = 1456.43\ \mu F \rightarrow C_{dc} = 1500\ \mu F \tag{3.2}$$

The coupling inductance is calculated in eq. (3.3) for a hysteresis band of $HB = 0.01\ A$ and inverter switching frequency of $f_i = 2000\ kHz$ according to eq. (2.21).

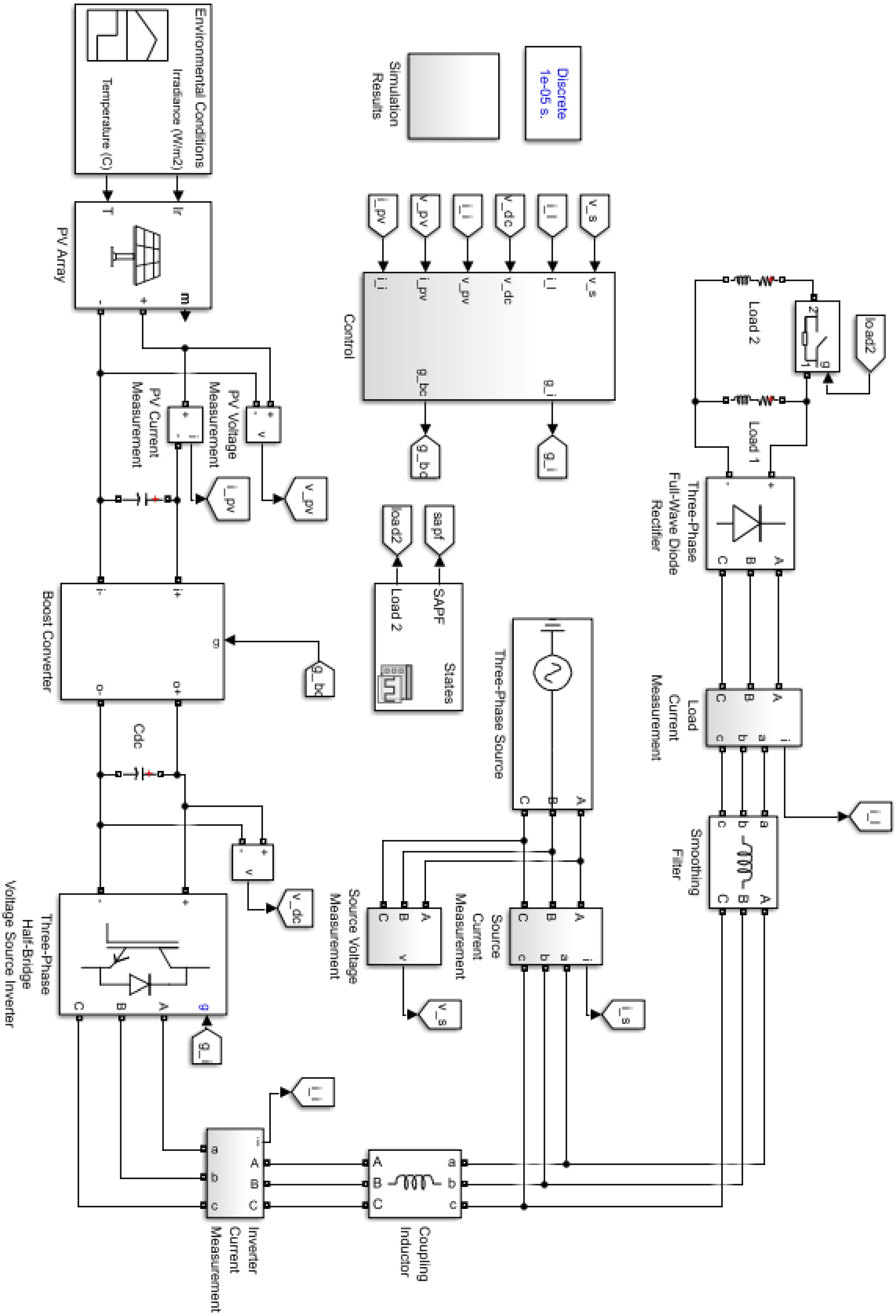

Figure 3.1: Simulink model of the proposed PV integrated grid-tied APF system

Table 3.1: System parameters in simulation study

Grid		$V_s = 400\,V, f_s = 50\,Hz$
Nonlinear loads	**1**	$R_{l,1} = 60\,\Omega, L_{l,1} = 80\,mH, P_{l,1} = 4.484kW$
	2	$R_{l,2} = 60\,\Omega, L_{l,2} = 80\,mH, P_{l,2} = 4.484\,kW$
Inverter		$L_i = 5\,mH$
DC-link		$C_{dc} = 1500\,\mu F, V_{dc}^* = 700\,V$
DC-DC boost converter		$L_b = 4\,mH$
PV module		$V_{pv,mpp,stc} = 328.2\,V,\ I_{pv,mpp,stc} = 10.98\,A, P_{pv,mpp,stc} = 3.603\,kW$

$$L_i = \frac{\sqrt{3} \times V_{dc}}{12 \times f_i \times HB} = \frac{\sqrt{3} \times 700}{12 \times 2000 \times 10\text{^}3 \times 0.01} = 5\,mH \tag{3.3}$$

The boost converter inductance is calculated in eq. (3.4) according to eq. (2.9) to limit the current ripples to 2.196 A i.e., 20 % of the rated PV current, $I_{pv,mpp,stc}$.

$$L_b = \frac{V_{pv,mpp,stc}(V_{dc}^* - V_{pv,mpp,stc})}{\Delta i_L f_b V_{dc}^*} = \frac{328.2 \times (700 - 328.2)}{2.196 \times 20 \times 10\text{^}3 \times 700} = 4\,mH \tag{3.4}$$

Two operational scenarios are considered for the simulation studies. For comparative analysis, the performances of the FLCs are evaluated against the conventional P&O based controller for MPPT and PI controller for DC link voltage regulation. The Simulink models of the blocks comprising the proposed and conventional controllers are shown in Fig. 3.2 and Fig. 3.3, respectively. The gains used for the input and output variables of the FLCs are $G_O = 0.06$, $G_{\Delta O} = 100$, $G_{\Delta D} = 0.06$, $G_E = 1$, $G_{dE} = 10$ and $G_p = 100$. The implementation of the P&O algorithm is done according to the Fig. 1.2.1.1 with fixed step size $\Delta D_{P\&O} = 0.0001$. The tuning of the PI controller is done according to the [22, eq. (14)-(15)]. The obtained proportional and integral coefficients are $K_p = 0.62$ and $K_i = 0.88$, respectively.

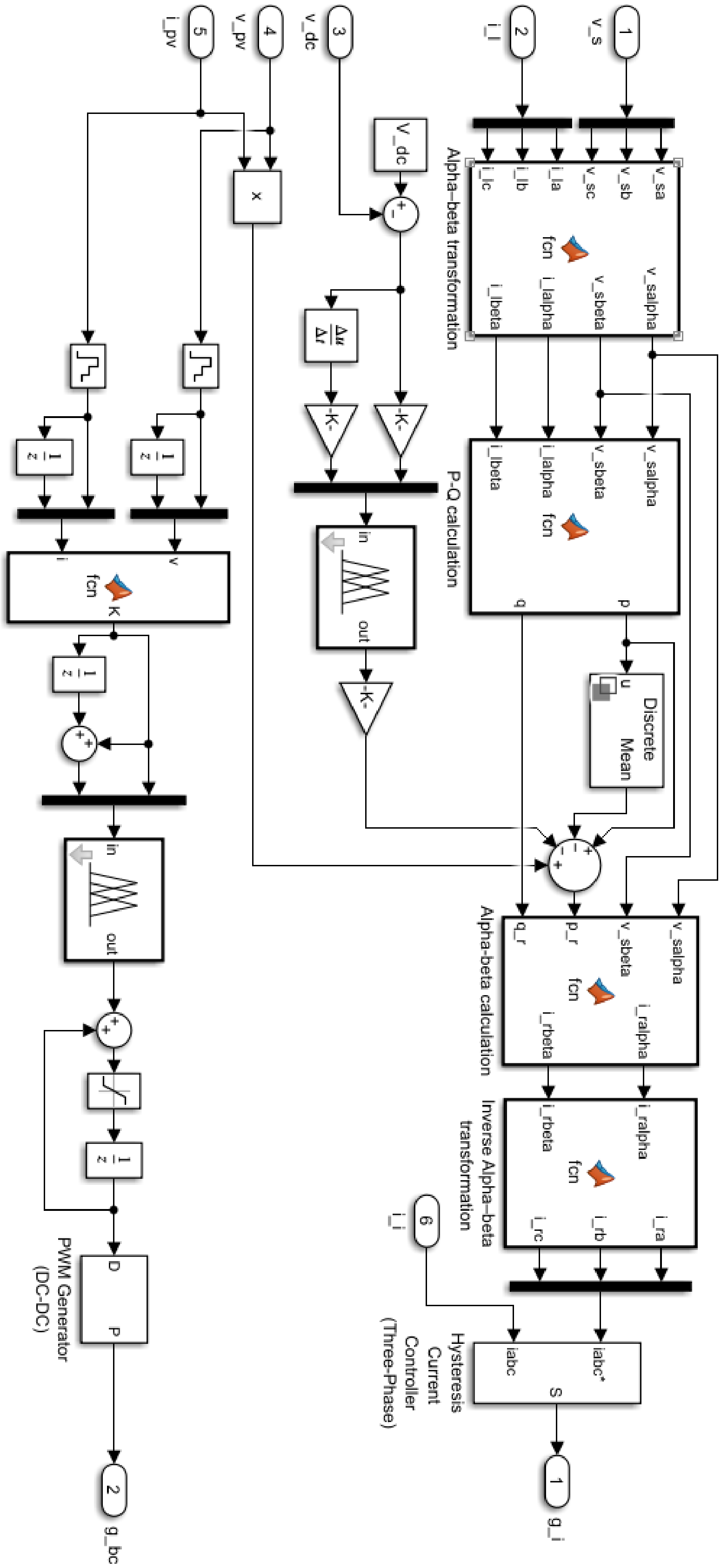

Figure 3.2: Simulink model for the proposed FLCs for MPPT and DC link voltage regulation

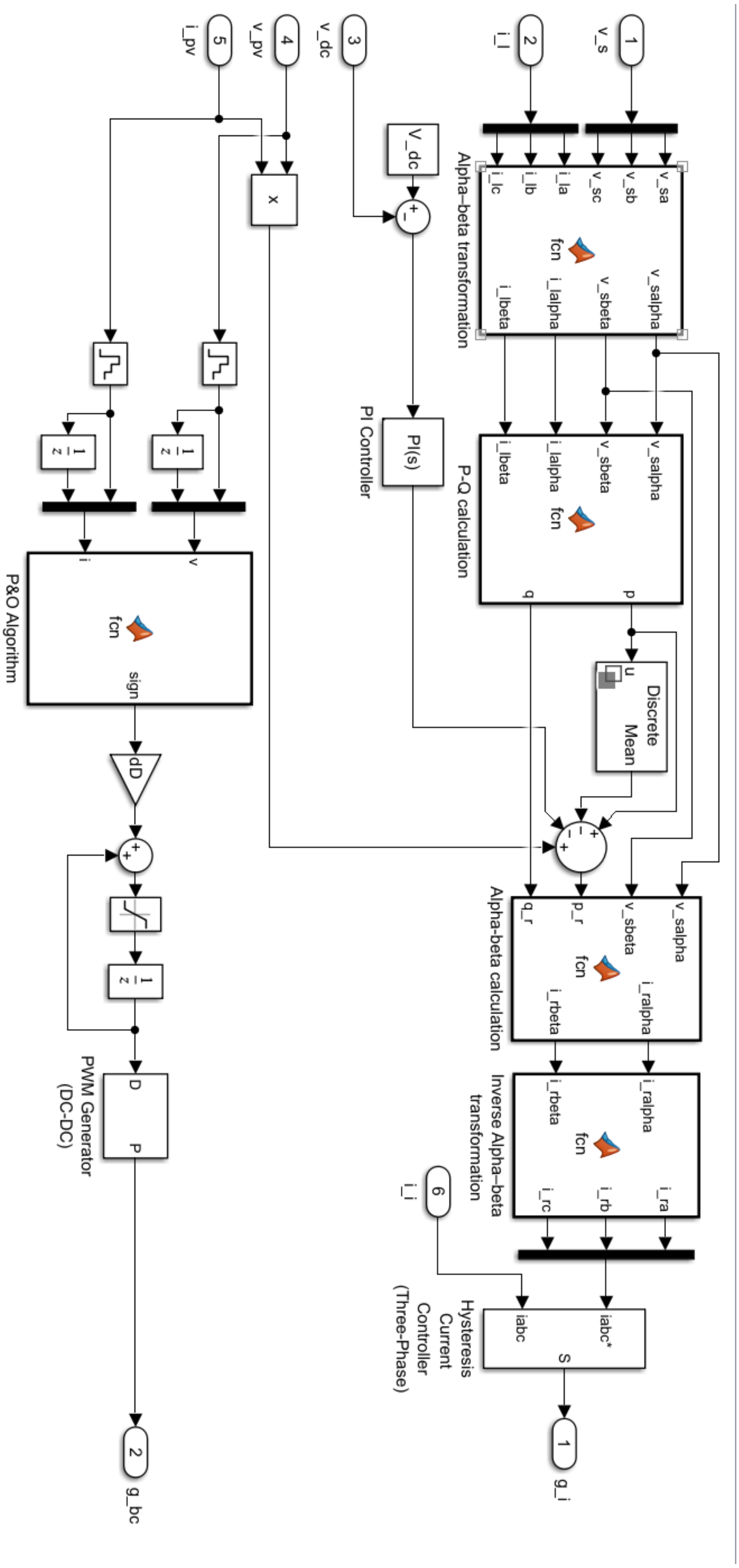

Figure 3.3: Simulink model for the conventional P&O-based MPPT and PI-based DC link voltage regulation

3.2. Varying Solar Irradiance

In the first scenario, the operation of the system is analyzed under dynamic changes in solar irradiance, G, at standard temperature, $T_{stc} = 25^{\circ}C$ and constant loading (Fig 3.4). Fig 3.5 shows the corresponding voltage and current waveforms of the system. Since a balanced

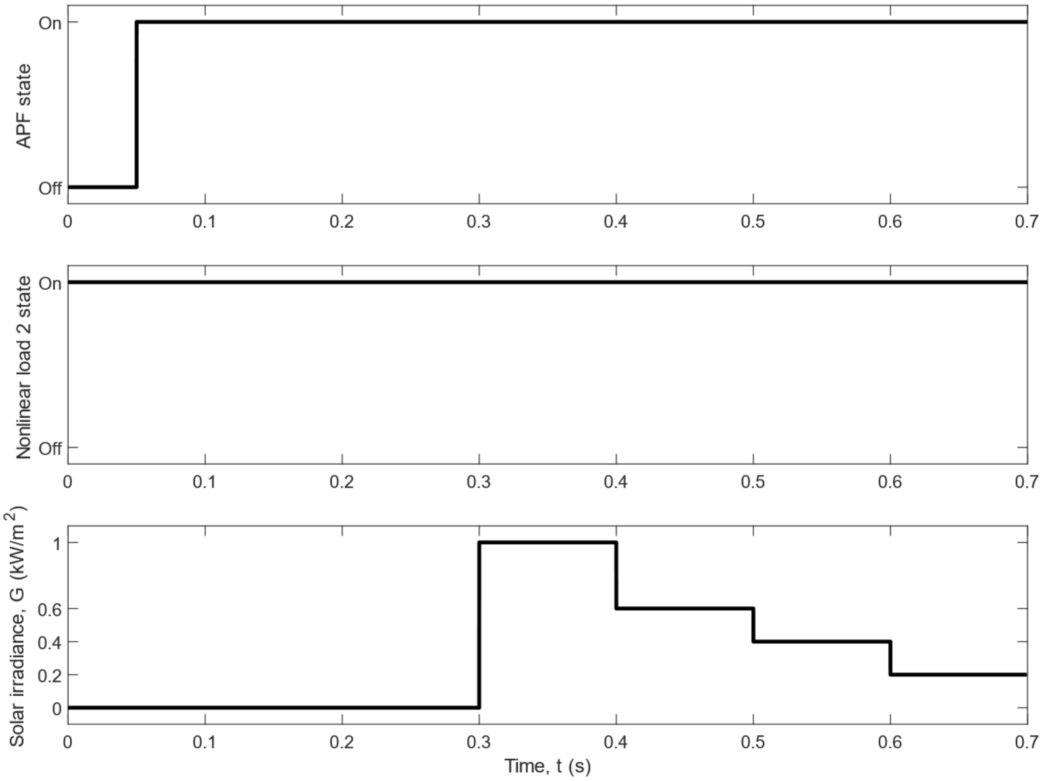

Figure 3.4: Operational scenario with dynamic changes in solar irradiance

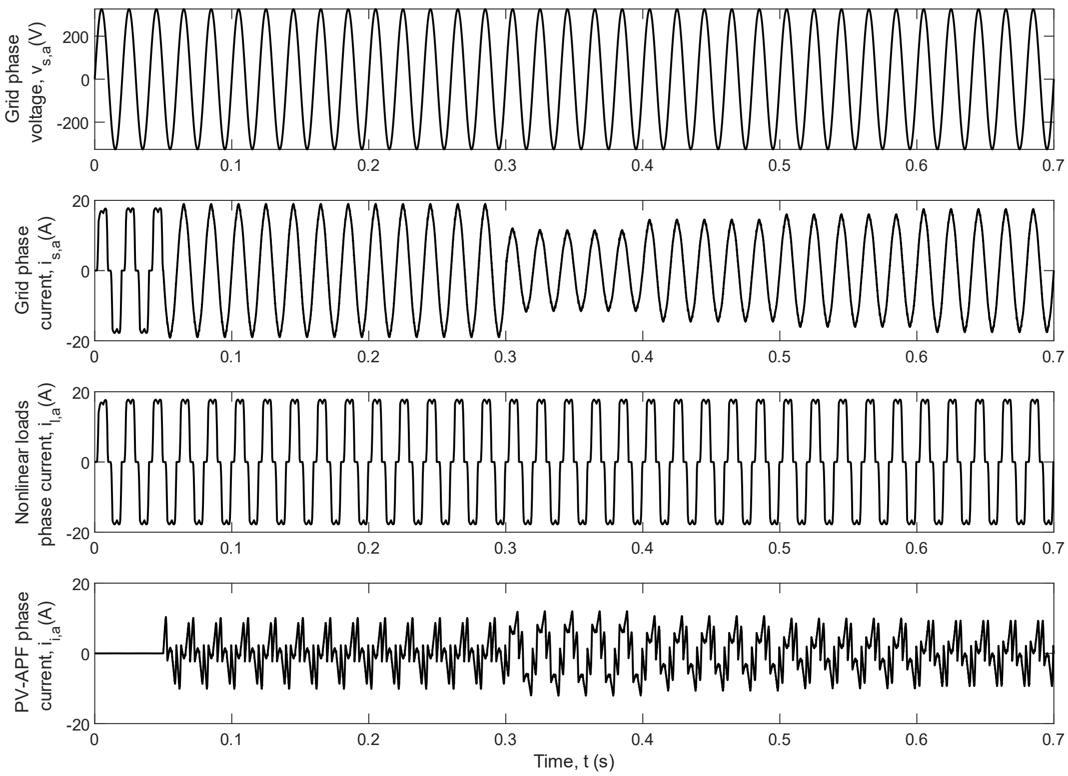

Figure 3.5: Voltage and current waveforms of the system in the scenario with dynamic changes in solar irradiance

three-phase system is considered in this work, voltage and current waveforms corresponding to only one of the phases are used for the analysis. The simulation starts with both APF and PV system turned off. As no PV power and compensation for the harmonics are generated, the active power demand of the load is entirely fed from the grid and the undesired harmonics from the nonlinear loads are circulated within the grid resulting in distorted supply current. Fig 3.6 (a) shows the fast Fourier transform analysis on the harmonic contents of the load and grid currents. The currents have harmonic orders of $h = 1, 5, 7, 11, 13\dots$ as expected from eq. (2.4) which result in THD of 22.88 %. At $t = 0.05\ s$, the APF is turned on and starts to generate compensation for the load current harmonics. The grid current waveform in this case takes sinusoidal shape with small-scale high-frequency ripples due to the HB of the hysteresis current controller. As a result, the THD is reduced to 2.10 % (Fig 3.6 (b)).

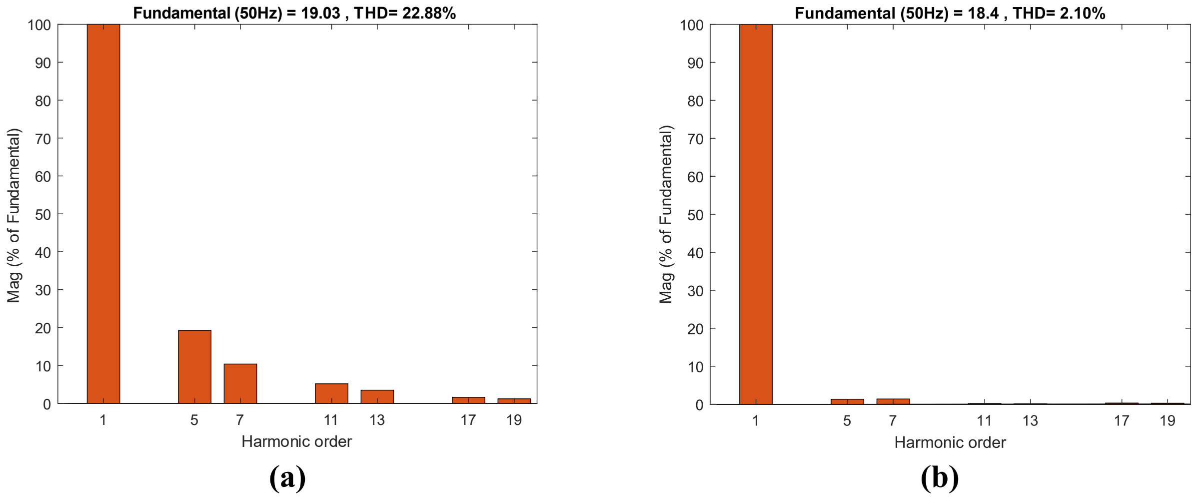

Figure 3.6: Harmonic contents of (a) load and grid currents before compensation and (b) grid current after APF compensation between t=0.05 s and t=0.3 s.

At $t = 0.3\ s$, the PV system is turned on at maximum irradiance i.e., $G = 1\ kW/m^2$ with following stepwise decreases in G to 0.6 kW/m^2 at $t = 0.4\ s$, 0.4 kW/m^2 at $t = 0.5\ s$ and 0.2 kW/m^2 at $t = 0.6\ s$. During these intervals, the active power demand of the loads, $P_l = 8.967\ kW$, is partially shared between the PV system and the grid. Fig. 3.7 compares the active power plots of the system in the cases of conventional controller with P&O algorithm and the proposed FLC for MPPT. The performances of the controllers are evaluated with regard to settling times and steady state-errors in response to the abrupt step changes in the G (Table 3.2). The settling time, t_{st}, is estimated as the time it takes for the active power supplied by the PV integrated APF, p_i, to converge to its steady state value within 5% tolerance. The steady-state errors, E_{ss}, are estimated as the absolute difference between the steady-state values and the theoretical maximum power of the PV module at the given G. It can be seen that the proposed FLC for MPPT shows shorter t_{st} and smaller E_{ss}. This is due to the fact that the conventional P&O algorithm uses small fixed increments/decrements in duty cycle, $\Delta D_{P\&O}$, for

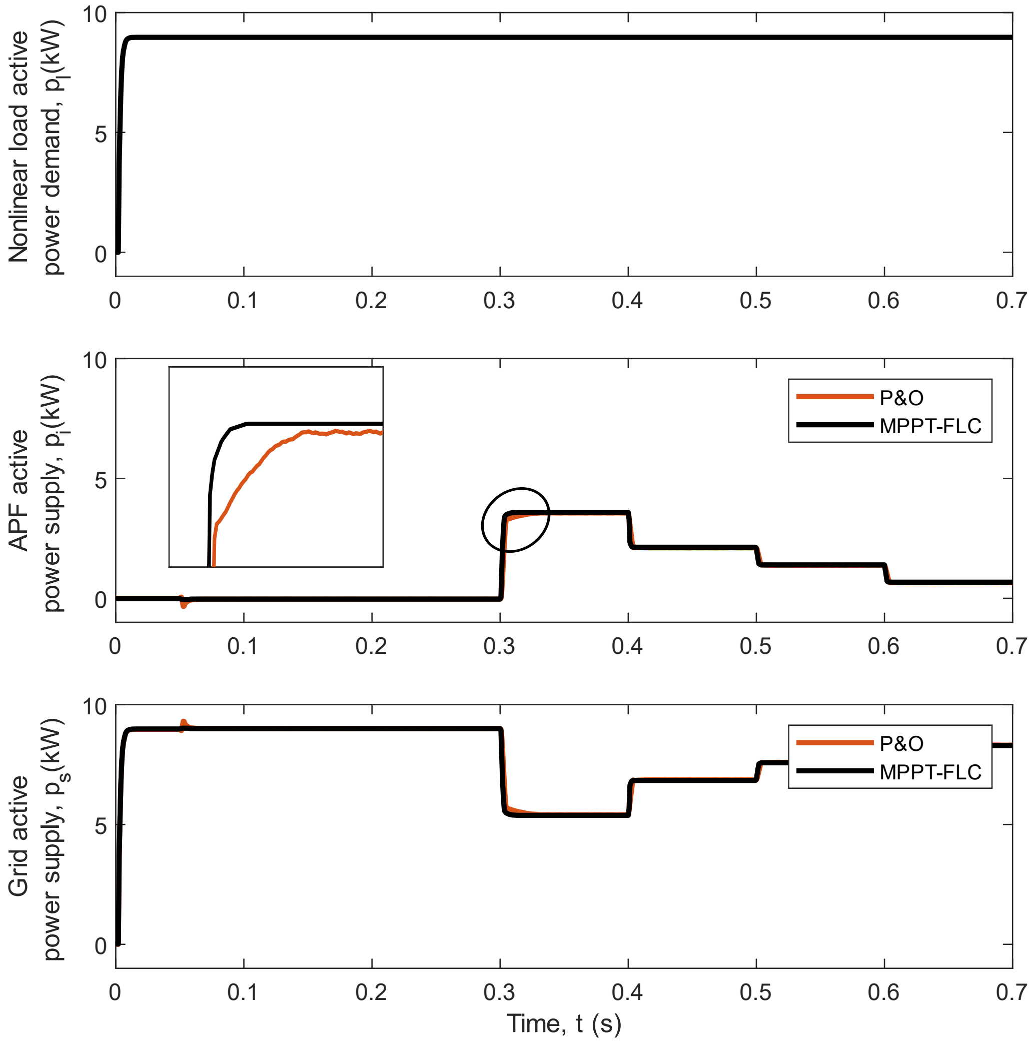

Figure 3.7: Active power waveforms of the system in the scenario with dynamic changes in solar irradiance.

tracking the MPP and thus responds relatively slow to sudden and large changes in G. Furthermore, due to the fixed $\Delta D_{P\&O}$, the P&O algorithm does not settle precisely at MPP, but instead continues to oscillate around it. The oscillations cause power losses, which in turn, result in lower PV efficiency [43-44]. Decreasing the $\Delta D_{P\&O}$ to reduce the oscillations will lead to longer t_{st}, while increasing the $\Delta D_{P\&O}$ for faster tracking will lead to larger oscillations and E_{ss}. The FLC, on the other hand, adaptively adjusts the ΔD based on the implemented rule-base and membership functions in response to the changes in the inputs. During the sudden

Table 3.2: Settling times and steady-state errors for the P&O based controller and FLC in the scenario with dynamic changes in solar irradiance.

		Solar Irradiance, G (kW/m^2)			
		1	0.6	0.4	0.2
P&O	t_{st} (ms)	13.3	3.45	2.98	2.98
	E_{ss} (W)	40.0	34.2	35.5	35.7
FLC	t_{st} (ms)	3.78	1.97	1.82	1.81
	E_{ss} (W)	15.5	12.6	21	18.7

change in G, FLC takes larger ΔD to reach the MPP, and once near the MPP, it takes smaller ΔD to minimize oscillations. As a result, it achieves higher tracking speed and accuracy.

The abrupt changes in the PV output create momentary differences between the active power supply and demand in the system. The differences are compensated by charging/discharging the DC link capacitor, C_{dc}, resulting in fluctuations of the DC link voltage, v_{dc}. These fluctuations, in turn, undermine the operation of the APF. Fig. 3.8 shows the v_{dc} waveforms in the cases of conventional PI controller and proposed FLC. The performances of the controllers are evaluated in terms of overshoot/undershoot, t_{st}, E_{ss}, and

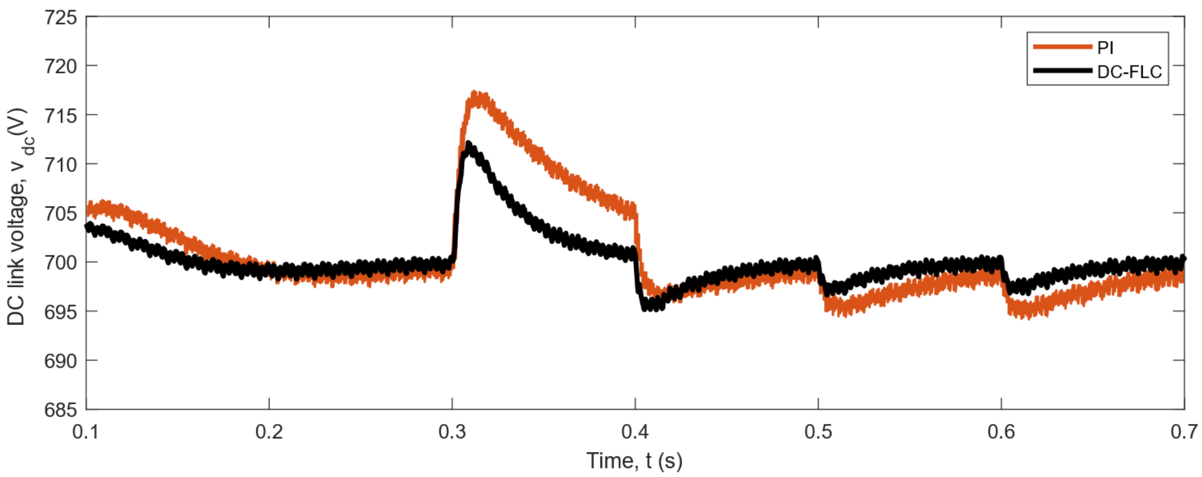

Figure 3.8: DC link voltage waveforms in the scenario with dynamic changes in solar irradiance.

grid current THD during the intervals of changes in the G (Table 3.3). In this case, t_{st} is estimated as the time it takes for the v_{dc} to converge to the reference value $V_{dc}^* = 700\ V$ within $\pm 2\ V$ tolerance and E_{ss} is estimated as the average absolute difference between the v_{dc} and the V_{dc}^* at the end of the given interval. The results show that the FLC achieves relatively faster and more accurate responses with less overshoots/undershoots compared to the PI controller which lead to more stable DC link voltage waveform and better harmonic compensation.

Table 3.3: DC link voltage overshoots/undershoots, settling times, steady-state errors and grid current THDs for the PI based controller and FLC in the scenario with dynamic changes in solar irradiance.

		Simulation time, t (s)			
		0.3-0.4	0.4-0.5	0.5-0.6	0.6-0.7
PI	Overshoot/Undershoot (%)	2.29	0.5	0.714	0.684
	t_{st} (ms)	-	73.3	81.0	79.9
	E_{ss} (mV)	5100	1322	1063	1058
	THD (%)	5.23	4.78	3.97	3.86
FLC	Overshoot/Undershoot (%)	1.57	0.77	0.423	0.421
	t_{st} (ms)	71.7	36.7	25.9	25.2
	E_{ss} (mV)	907	133	97	78
	THD (%)	3.03	2.51	2.33	2.20

3.3. Varying Loading

In the second scenario, the operation of the system is analyzed under dynamic changes in the loading, while PV system once activated at $t = 0.2\ s$ stays at constant $G = 1\ kW/m^2$ (Fig 3.9). Fig 3.10 shows the corresponding voltage and current waveforms of the system. Initially, both loads are connected the active power demand of which is partially shared between the PV module and the grid. From $t = 0.4\ s$ to $t = 0.6\ s$, the load 2 is disconnected. The decrease in the active power demand is balanced by the decrease in the current and the active power supplied from the grid. Since active power supplied by the PV stays the same, the changes in the loading do not have a significant effect on the performance of the MPPT control. However, as in the first scenario, at the points of abrupt changes in the loading

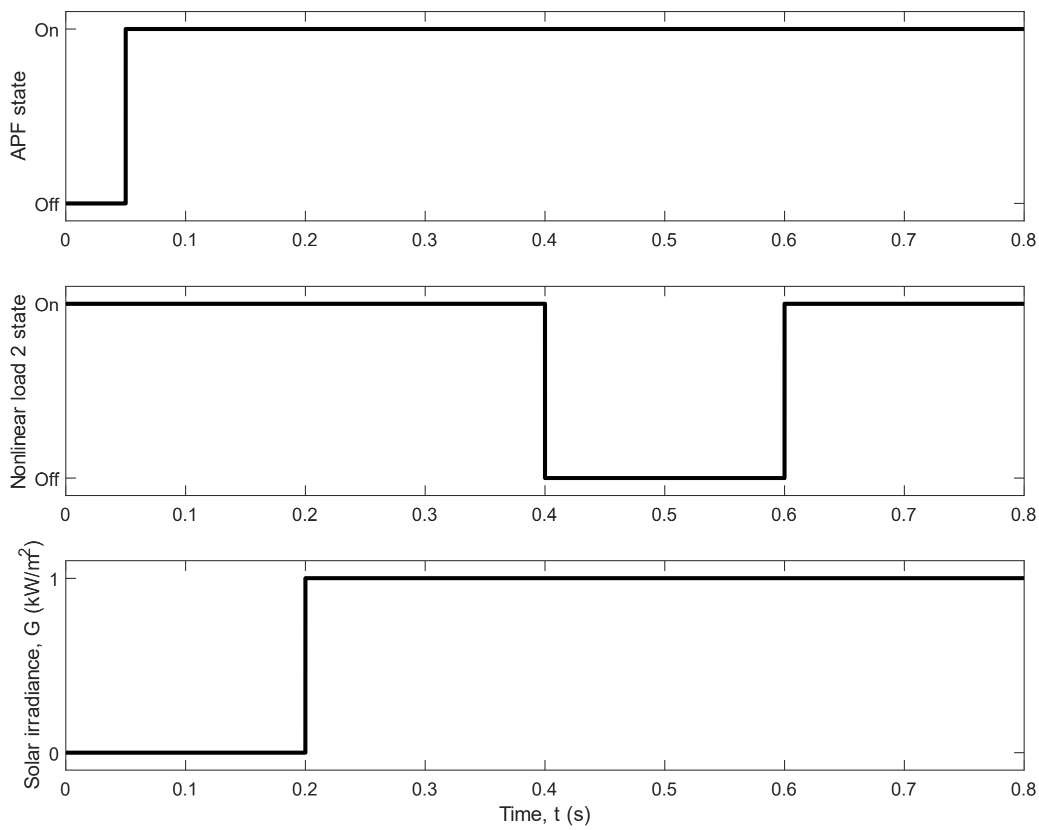

Figure 3.9: Operational scenario with dynamic changes in the loading

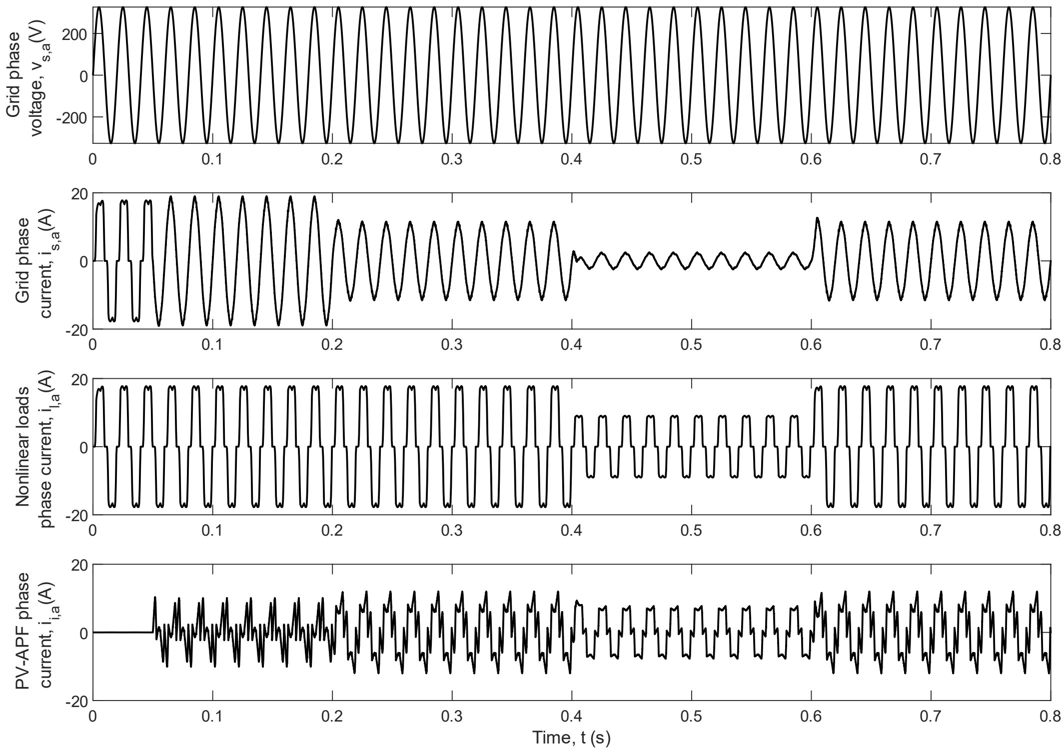

Figure 3.10: Voltage and current waveforms of the system in the scenario with dynamic changes in the loading

momentary differences between the active power supply and demand in the system arise which are compensated by the C_{dc} resulting in fluctuations of the v_{dc} waveforms and hindrances to the operation of the APF. Fig. 3.11 shows the v_{dc} waveforms in the cases of conventional PI controller and proposed FLC. Table 3.4 tabulates the performances of the controllers in terms DC link voltage overshoots/undershoots, settling times, steady-state errors and grid current THDs during the intervals of changes in the load. In this case $\pm 1\ V$ tolerance range is used for estimating t_{st} . The results show that both controllers were able to minimize the $\mathrm{E_{ss}}$. However, as in the first scenario, the FLC achieves faster t_{st} with less overshoots/undershoots compared to the PI controller which lead to more stable DC link voltage waveform and better harmonic compensation.

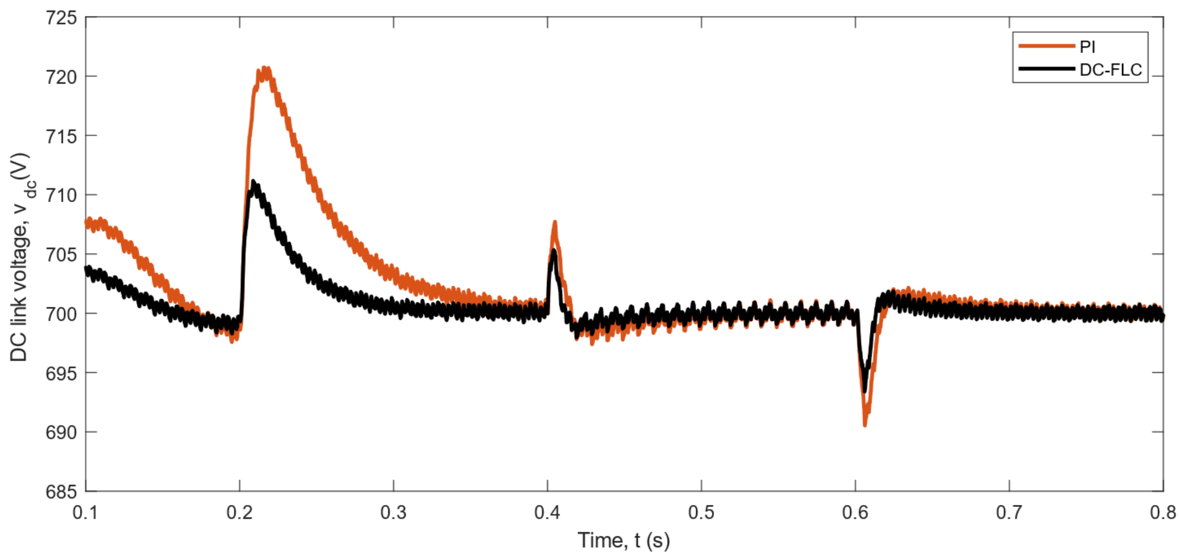

Figure 3.11: DC link voltage waveforms in the scenario with dynamic changes in the loading.

Table 3.4: DC link voltage overshoots/undershoots, settling times, steady-state errors and grid current THDs for the PI based controller and FLC in the scenario with dynamic changes in the loading.

		Simulation time, t (s)	
		$0.4 - 0.6$	$0.6 - 0.8$
PI	Overshoot/Undershoot (%)	1.10	1.35
	$t_{settling}$ (ms)	59.15	64.7
	$E_{steady-state}$ (mV)	0	0
	THD (%)	7.42	5.75
FLC	Overshoot/Undershoot (%)	0.709	0.944
	$t_{settling}$ (ms)	28.11	36.4
	$E_{steady-state}$ (mV)	0	0
	THD (%)	4.86	3.05

Chapter 4 – Experimental Results

4.1. Details of Setup

Experimental test is carried out in a laboratory setup to validate the effectiveness of the PV Integrated APF system (Fig. 4.1). The designed controllers are implemented on the FPGA-based WAVECT WCU300HD controller. The advantage of using the WAVECT is that it can produce a real-time executable code directly from the designed MATLAB-Simulink models allowing for fast control prototyping. The WAVECT also provides build-in voltage and current sensors and PWM channels for direct measurement of the feedback signals and control of the converters without the need for external circuity. The test is performed with SM-SPV002-5020 1 kW PV emulator and an 2 kW DC load.

4.2. Results and Discussion

The experimental results with system voltage and current waveforms are presented in Fig 4.2.

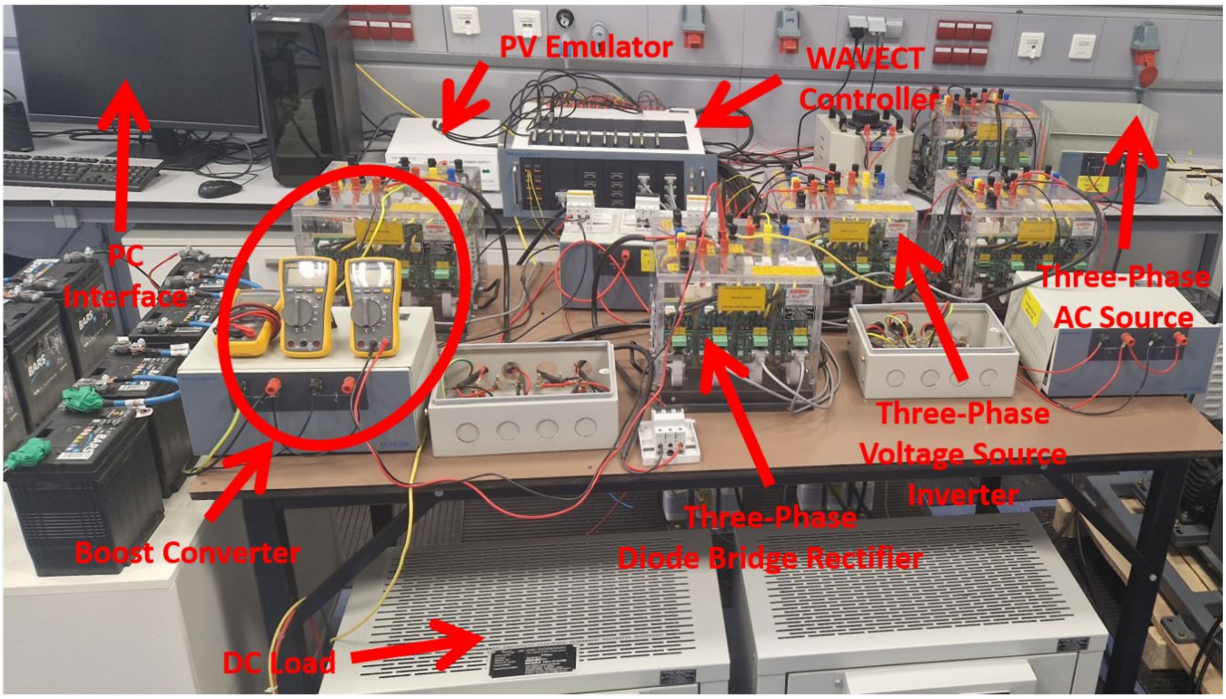

Figure 4.1: Experimental laboratory setup for the proposed PV Integrated APF system

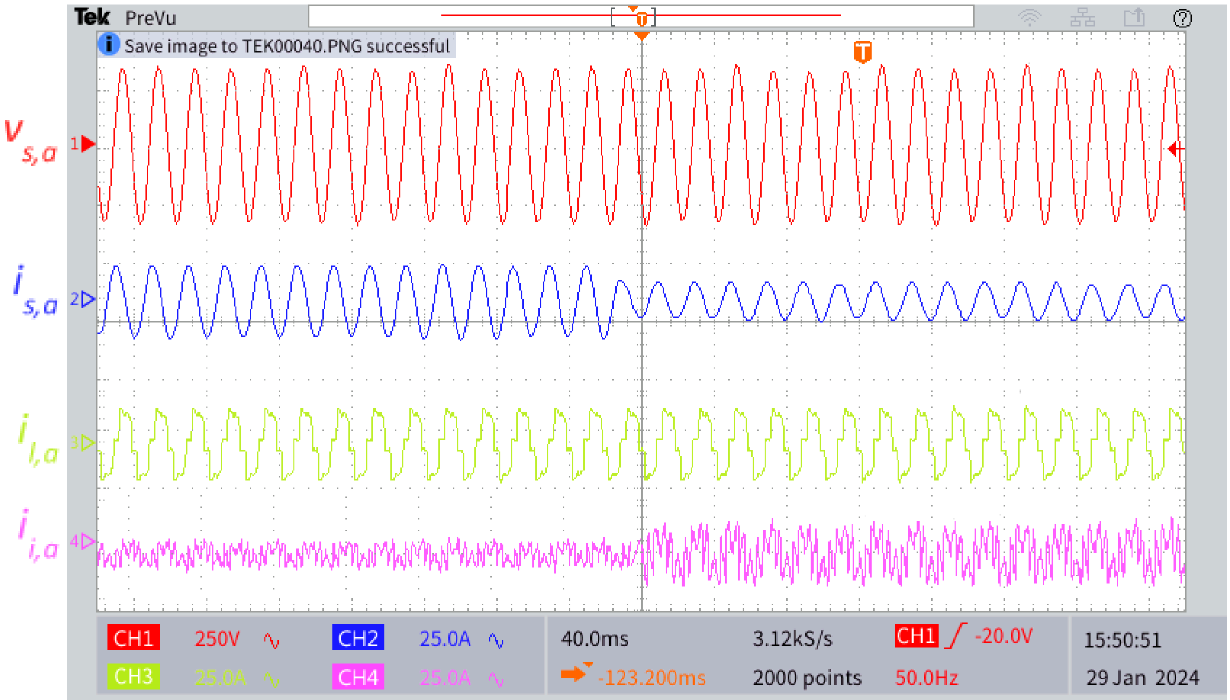

Figure 4.2: Experimental results illustrating the operation of the PV integrated APF

At first, the PV injection is turned off and the APF operated by generating compensation for the load current harmonics while active power demand of the load is entirely fed from the grid. Then PV injection is turned on with $G = 1\ kW/m^2$. The active power demand of the load in this case is partially shared between the PV system and the grid. The Fig. 4.3-4.5 show the harmonic content of the load and grid currents during this interval. It can be seen that in the case of FLCs, the PV integrated APF achieved grid current THD reduction from 26.99 % to 4.19 % which is below the 5 % limit indicated in the IEEE 519 standard. On the other hand, in the case of conventional P&O and PI controllers the THD is 5.47 %.

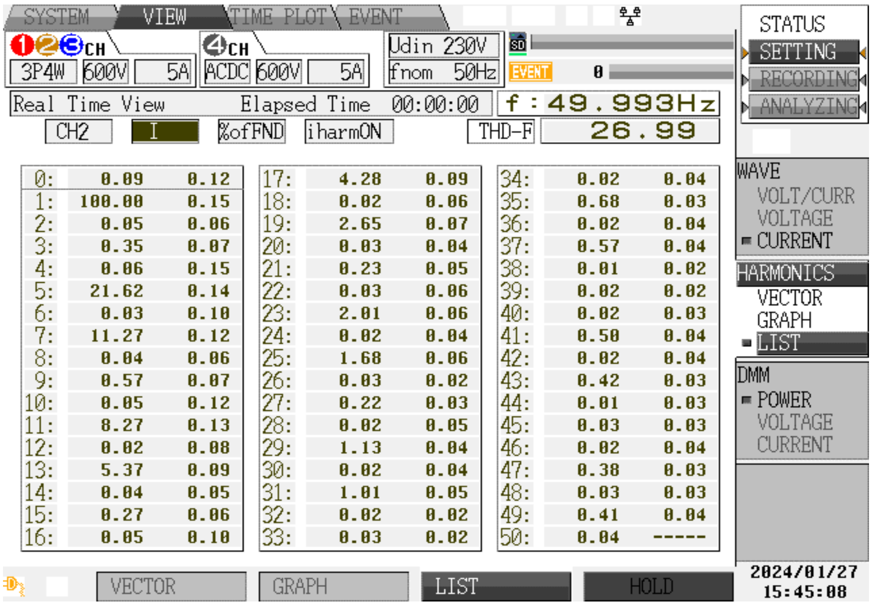

0:	0.09	0.12	17:	4.28	0.09	34:	0.02	0.04
1:	100.00	0.15	18:	0.02	0.06	35:	0.68	0.03
2:	0.05	0.06	19:	2.65	0.07	36:	0.02	0.04
3:	0.35	0.07	20:	0.03	0.04	37:	0.57	0.04
4:	0.06	0.15	21:	0.23	0.05	38:	0.01	0.02
5:	21.62	0.14	22:	0.03	0.06	39:	0.02	0.02
6:	0.03	0.10	23:	2.01	0.06	40:	0.02	0.03
7:	11.27	0.12	24:	0.02	0.04	41:	0.50	0.04
8:	0.04	0.06	25:	1.68	0.06	42:	0.02	0.04
9:	0.57	0.07	26:	0.03	0.02	43:	0.42	0.03
10:	0.05	0.12	27:	0.22	0.03	44:	0.01	0.03
11:	8.27	0.13	28:	0.02	0.05	45:	0.03	0.03
12:	0.02	0.08	29:	1.13	0.04	46:	0.02	0.04
13:	5.37	0.09	30:	0.02	0.04	47:	0.38	0.03
14:	0.04	0.05	31:	1.01	0.05	48:	0.03	0.03
15:	0.27	0.06	32:	0.02	0.02	49:	0.41	0.04
16:	0.05	0.10	33:	0.03	0.02	50:	0.04	-----

Figure 4.3: Harmonic content of the load current

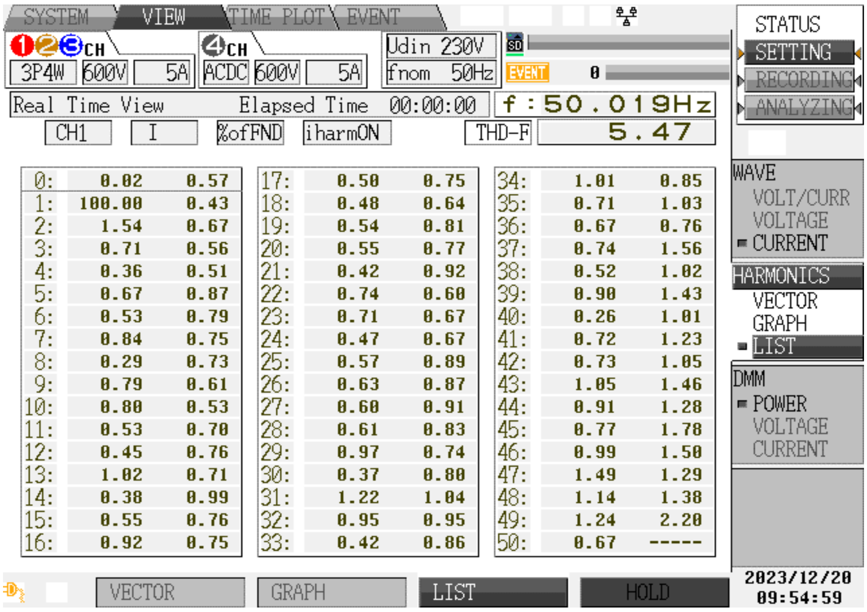

0:	0.02	0.57	17:	0.50	0.75	34:	1.01	0.85
1:	100.00	0.43	18:	0.48	0.64	35:	0.71	1.03
2:	1.54	0.67	19:	0.54	0.81	36:	0.67	0.76
3:	0.71	0.56	20:	0.55	0.77	37:	0.74	1.56
4:	0.36	0.51	21:	0.42	0.92	38:	0.52	1.02
5:	0.67	0.87	22:	0.74	0.60	39:	0.90	1.43
6:	0.53	0.79	23:	0.71	0.67	40:	0.26	1.01
7:	0.84	0.75	24:	0.47	0.67	41:	0.72	1.23
8:	0.29	0.73	25:	0.57	0.89	42:	0.73	1.05
9:	0.79	0.61	26:	0.63	0.87	43:	1.05	1.46
10:	0.80	0.53	27:	0.60	0.91	44:	0.91	1.28
11:	0.53	0.70	28:	0.61	0.83	45:	0.77	1.78
12:	0.45	0.76	29:	0.97	0.74	46:	0.99	1.50
13:	1.02	0.71	30:	0.37	0.80	47:	1.49	1.29
14:	0.38	0.99	31:	1.22	1.04	48:	1.14	1.38
15:	0.55	0.76	32:	0.95	0.95	49:	1.24	2.20
16:	0.92	0.75	33:	0.42	0.86	50:	0.67	-----

Figure 4.4: Harmonic content of the grid current in case of conventional P&O and PI controllers

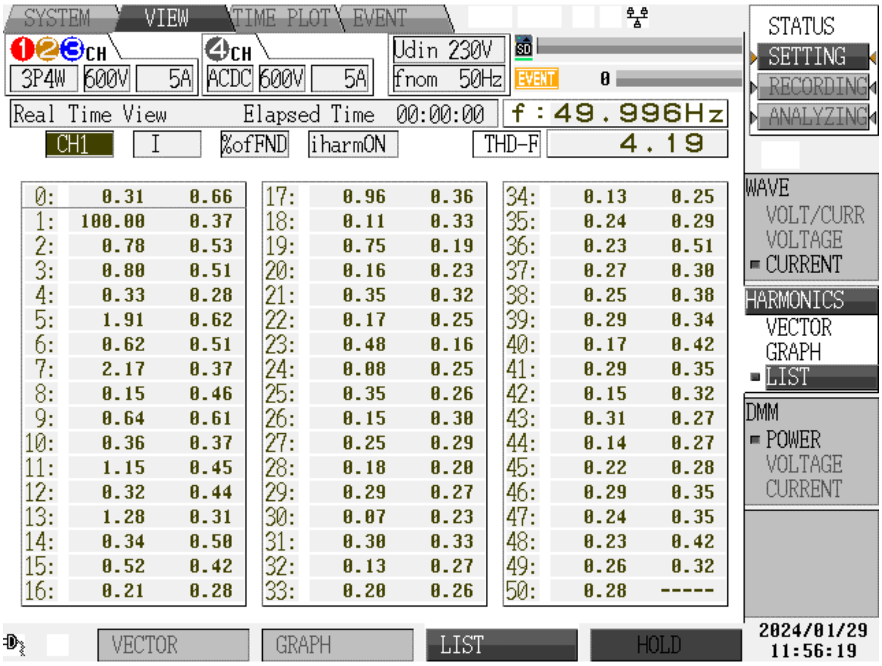

Figure 4.5: Harmonic content of the grid current in case of proposed FLCs

Chapter 5 - Conclusion

5.1. Summary of Work Done

In this MSc thesis, PV integrated grid-tied APF system was designed and developed to provide dual benefits of supplying PV power to nonlinear loads and reducing the grid current harmonic distortion. Two FLCs for MPPT and DC link voltage regulation were proposed to maximize the PV system efficiency and reduce the fluctuations in the DC link under dynamic environmental and loading conditions. Simulation studies and experimental tests were done in MATLAB/Simulink and laboratory setup to evaluate and validate the operation of the proposed system. The simulation results show that the designed FLCs provide more accurate and faster response compared to the conventional P&O and PI controllers under large and abrupt changes in the solar insolation and loading resulting in higher PV efficiency and harmonic compensation capability. The experimental test confirmed that the PV integrated APF was able to supply PV active power to the load and achieve grid current THD within the limit specified in the IEEE 519 standard. The obtained results will promote wider adoption of PVs and APFs in the energy sector and contribute to mitigating the carbon emissions, energy shortage and PQ issues.

5.2. Future Work

In this MSc thesis, a fixed hysteresis band current control was used that results in large spectrum of high-frequency current ripples. Future works can include designing FLC for adaptive current control to further improve the performance of the PV integrated APF. Also, the PV integrated APF system was designed and evaluated with non-shaded PV and balanced loading conditions. Thus, there is a need for further research on design considerations and performance analysis in the more practical cases of partial PV shading and unbalanced loading. Furthermore, this work adopted shunt APF for current harmonic compensation. The future research scope in this direction can be extended to APFs with different topologies i.e., series or hybrid and for mitigating other PQ issues e.g., power factor correction, load balancing and voltage harmonic compensation.

Bibliography

[1] "Statistical Review of World Energy," Energy Institute, 2024. Accessed: Apr. 10, 2025. [Online]. Available: https://www.energyinst.org/statistical-review.

[2] R. B. Bollipo, S. Mikkili, and P. K. Bonthagorla, "Critical review on PV MPPT techniques: classical, intelligent and optimisation," IET Renewable Power Generation, vol. 14, pp. 1433-1452, 2020, doi: 10.1049/iet-rpg.2019.1163.

[3] Eltawil, M.A. and Zhao, Z. (2013) 'MPPT techniques for photovoltaic applications', Renewable and Sustainable Energy Reviews, 25, pp. 793–813. doi:10.1016/j.rser.2013.05.022.

[4] Bendib, B., Belmili, H. and Krim, F. (2015) 'A survey of the most used MPPT methods: Conventional and advanced algorithms applied for Photovoltaic Systems', Renewable and Sustainable Energy Reviews, 45, pp. 637–648. doi:10.1016/j.rser.2015.02.009.

[5] Sarvi, M. and Azadian, A. (2021) 'A comprehensive review and classified comparison of MPPT algorithms in PV systems', Energy Systems, 13(2), pp. 281–320. doi:10.1007/s12667-021-00427-x.

[6] Mao, M. et al. (2020) 'Classification and summarization of solar photovoltaic MPPT techniques: A review based on traditional and Intelligent Control Strategies', Energy Reports, 6, pp. 1312–1327. doi:10.1016/j.egyr.2020.05.013.

[7] "IEEE Standard for Harmonic Control in Electric Power Systems," in IEEE Std 519-2022 (Revision of IEEE Std 519-2014), pp.1-31, 5 Aug. 2022, doi: 10.1109/IEEESTD.2022.9848440.

[8] Patil, B. and Pawar, V.S. (2017) 'Power Quality Effects on Nonlinear Loads ', International Research Journal of Engineering and Technology, 04(06), pp. 3244–3247.

[9] Li, D. et al. (2021) 'A comprehensive review of improving power quality using active power filters', Electric Power Systems Research, 199, p. 107389. doi:10.1016/j.epsr.2021.107389.

[10] Das, S.R. et al. (2021) A comprehensive survey on different control strategies and applications of active power filters for power quality improvement, MDPI. Available at: https://www.mdpi.com/1996-1073/14/15/4589 (Accessed: 14 March 2024).

[11] Hoon, Y. et al. (2017) 'Control algorithms of shunt active power filter for harmonics mitigation: A Review', Energies, 10(12), p. 2038. doi:10.3390/en10122038.

[12] L. Shang, H. Guo, and W. Zhu, "An improved MPPT control strategy based on incremental conductance algorithm," Protection and Control of Modern Power Systems, vol. 5, no. 14, 2020, doi: 10.1186/s41601-020-00161-z.

[13] I. Owusu-Nyarko, M. A. Elgenedy, I. Abdelsalam, and K. H. Ahmed, "Modified Variable Step-Size Incremental Conductance MPPT Technique for Photovoltaic Systems," Electronics, vol. 10, no. 19, p. 2331, 2021, doi: 10.3390/electronics10192331.

[14] Li, C. et al. (2016) 'A high-performance adaptive incremental conductance MPPT algorithm for Photovoltaic Systems', Energies, 9(4), p. 288. doi:10.3390/en9040288.

[15] G. Calvinho, J. Pombo, S. Mariano and M. d. Rosario Calado, "Design and Implementation of MPPT System Based on PSO Algorithm," 2018 International Conference on Intelligent Systems (IS), Funchal, Portugal, 2018, pp. 733-738, doi: 10.1109/IS.2018.8710479.

[16] R. Sridhar, C. Subramani, and S. Pathy, "A grasshopper optimization algorithm aided maximum power point tracking for partially shaded photovoltaic systems," Computers & Electrical Engineering, vol. 92, p. 107124, Jun. 2021. doi:10.1016/j.compeleceng.2021.107124

[17] Saad, W., Hegazy, E. and Shokair, M. (2022) 'Maximum power point tracking based on modified Firefly Scheme for PV system', SN Applied Sciences, 4(4). doi:10.1007/s42452-022-04976-3.

[18] Y. Zhao, A. An, Y. Xu, Q. Wang and M, Wang, "Model predictive control of grid-connected PV power generation system considering optimal MPPT control of PV module," Protection and Control of Modern Power Systems, vol. 6, no. 32, 2021, doi: 10.1186/s41601-021-00210-1.

[19] N. Kacimi, A. Idir, S. Grouni and M. S. Boucherit, "Improved MPPT Control Strategy for PV Connected to Grid Using IncCond-PSO-MPC Approach," in CSEE Journal of Power and

Energy Systems, vol. 9, no. 3, pp. 1008-1020, May 2023, doi: 10.17775/CSEEJPES.2021.08810.

[20] M. Ahmed, I. Harbi, R. Kennel, J. Rodríguez and M. Abdelrahem, "Maximum Power Point Tracking-Based Model Predictive Control for Photovoltaic Systems: Investigation and New Perspective," Sensors (Basels), vol. 22, no. 8, p. 3069, 2022, doi: 10.3390/s22083069.

[21] Chaoui, A. et al. (2007) 'Pi controlled three-phase shunt active power filter for power quality improvement', Electric Power Components and Systems, 35(12), pp. 1331–1344. doi:10.1080/15325000701426062.

[22] A. A. Imam, R. Sreerama Kumar, and Y. A. Al-Turki, "Modeling and Simulation of a PI Controlled Shunt Active Power Filter for Power Quality Enhancement Based on P-Q Theory," Electronics, vol. 9, no. 4, p. 637, Apr. 2020, doi: 10.3390/electronics9040637.

[23] W. Yeetum and V. Kinnares, "PI Controller Based on Direct Synthesis Method for DC-Link Voltage Control of Active Power Filter," 2018 International Electrical Engineering Congress (iEECON), Krabi, Thailand, 2018, pp. 1-4, doi: 10.1109/IEECON.2018.8712250.

[24] A. Talebkhah, M. S. Shadlu and S. Majid Fatemi, "Control Strategy of a Single Phase Active Power Filter with Adjustable DC Link Capacitor Voltage for THD Reduction in Non-linear Loads," 2019 10th International Power Electronics, Drive Systems and Technologies Conference (PEDSTC), Shiraz, Iran, 2019, pp. 606-611, doi: 10.1109/PEDSTC.2019.8697234.

[25] Benchouia, M.T. et al. (2014) 'Design and implementation of sliding mode and PI controllers based control for three phase shunt active power filter', Energy Procedia, 50, pp. 504–511. doi:10.1016/j.egypro.2014.06.061.

[26] S. D. Yusuf, A. Z. Loko, J. Abdullahi, and A. A. Abdulhamid, "Performance analysis of three-phase shunt active power filter for harmonic mitigation," Asian Journal of Research and Reviews in Physics, pp. 7–24, Oct. 2022. doi:10.9734/ajr2p/2022/v6i3118.

[27] N. D. Tuyen and G. Fujita, "PV-Active Power Filter Combination Supplies Power to Nonlinear Load and Compensates Utility Current," in IEEE Power and Energy Technology Systems Journal, vol. 2, no. 1, pp. 32-42, March 2015, doi: 10.1109/JPETS.2015.2404355.

[28] A. K. Mishra, S. R. Das, P. K. Ray, R. K. Mallick, A. Mohanty and D. K. Mishra, "PSO-GWO Optimized Fractional Order PID Based Hybrid Shunt Active Power Filter for Power Quality Improvements," IEEE Access, vol. 8, pp. 74497-74512, 2020, doi: 10.1109/ACCESS.2020.2988611.

[29] T. Demirdelen, R. I. Kayaalp and M. Tümay, "PSO-PI Based DC Link Voltage Control Technique for Shunt Hybrid Active Power Filter," 2016 International Conference on Systems Informatics, Modelling and Simulation (SIMS), Riga, Latvia, 2016, pp. 97-102, doi: 10.1109/SIMS.2016.18.

[30] S. Bosch, J. Staiger and H. Steinhart, "Predictive Current Control for an Active Power Filter With LCL-Filter," IEEE Transactions on Industrial Electronics, vol. 65, no. 6, pp. 4943-4952, 2018, doi: 10.1109/TIE.2017.2772176.

[31] K. Y. Yap, C. R. Sarimuthu and J. M. -Y. Lim, "Artificial Intelligence Based MPPT Techniques for Solar Power System: A review," in Journal of Modern Power Systems and Clean Energy, vol. 8, no. 6, pp. 1043-1059, November 2020, doi: 10.35833/MPCE.2020.000159.

[32] C. G. Villegas-Mier et al., "Artificial neural networks in MPPT algorithms for optimization of Photovoltaic Power Systems: A Review," Micromachines, vol. 12, no. 10, p. 1260, Oct. 2021. doi:10.3390/mi12101260.

[33] O. Boubaker, "MPPT techniques for photovoltaic systems: A systematic review in current trends and recent advances in Artificial Intelligence," Discover Energy, vol. 3, no. 1, Dec. 2023. doi:10.1007/s43937-023-00024-2.

[34] Salam, Z., Ahmed, J. and Merugu, B.S. (2013) 'The application of soft computing methods for MPPT of PV system: A technological and Status Review', Applied Energy, 107, pp. 135–148. doi:10.1016/j.apenergy.2013.02.008.

[35] O. Lahmadi and L. Benfarhi, "Different Artificial Intelligence Strategies to control an inverter of an active power filter for power quality improvement," International Journal of Power Electronics, vol. 12, no. 4, p. 399, 2020. doi:10.1504/ijpelec.2020.10032254.

[36] E. Mhawi, H. Daniyal, and M. H. Sulaiman, “Advanced techniques in harmonic suppression via active Power Filter: A Review,” International Journal of Power Electronics and Drive Systems (IJPEDS), vol. 6, no. 2, p. 185, Jun. 2015. doi:10.11591/ijpeds.v6.i2.pp185-195.

[37] B. Hauke, “Basic Calculation of a Boost Converter's Power Stage,” Texas Instruments, Nov. 2009. Accessed: Apr. 10, 2025. [Online]. Available: https://www.ti.com/lit/pdf/SLVA372.

[38] Y. Hoon, M. Mohd Radzi, M. Hassan, and N. Mailah, “DC-link capacitor voltage regulation for three-phase three-level inverter-based shunt active power filter with inverted error deviation control,” Energies, vol. 9, no. 7, p. 533, Jul. 2016. doi:10.3390/en9070533

[39] Soo Yeong Yi and Myung Jin Chung, "Stability analysis of a fuzzy logic controller for an uncertain dynamic system," Proceedings of 1994 IEEE 3rd International Fuzzy Systems Conference, Orlando, FL, USA, 1994, pp. 1028-1034 vol.2, doi: 10.1109/FUZZY.1994.343877.

[40] Y. Wang, Y. Wang, S.-Z. Chen, G. Zhang, and Y. Zhang, “A simplified minimum DC-link voltage control strategy for shunt active power filters,” Energies, vol. 11, no. 9, p. 2407, Sep. 2018. doi:10.3390/en11092407.

[41] V. Gali, P. K. Jamwal, N. Gupta, and A. Kumar, “Multimode Control Strategy to improve the power quality and autonomy of PV-Wind-Bess based microgrid using harmonic frequency adaptive observer filter,” Electric Power Systems Research, vol. 225, p. 109786, Dec. 2023. doi:10.1016/j.epsr.2023.109786.

[42] P. Gonzalez-Castrillo, E. Romero-Cadaval, M. Milanes-Montero, F. Barrero-Gonzalez and M. Guerrero-Martinez, "A new criterion for selecting the inductors of an Active Power Line Conditioner", Proc. (CPE), pp. 167-172, 2011.

[43] M. Killi and S. Samanta, "An Adaptive Voltage-Sensor-Based MPPT for Photovoltaic Systems With SEPIC Converter Including Steady-State and Drift Analysis," in IEEE Transactions on Industrial Electronics, vol. 62, no. 12, pp. 7609-7619, Dec. 2015, doi: 10.1109/TIE.2015.2458298.

[44] U. Yilmaz, O. Turksoy, and A. Teke, “Improved MPPT method to increase accuracy and speed in photovoltaic systems under variable atmospheric conditions,” International Journal of Electrical Power & Energy Systems, vol. 113, pp. 634–651, Dec. 2019. doi:10.1016/j.ijepes.2019.05.074